Journal of Computational Neuroscience
https://doi.org/10.1007/s10827-023-00853-z

RESEARCH

Transmission of delta band (0.5-4 Hz) oscillations from the globus pallidus to the substantia nigra pars reticulata in dopamine depletion

Timothy C. Whalen[1,2,3,4] · **John E. Parker**[1,3] · **Aryn H. Gittis**[2,3] · **Jonathan E. Rubin**[1,3]

Received: 20 January 2023 / Revised: 20 January 2023 / Accepted: 28 April 2023

Abstract

Parkinson's disease (PD) and animal models of PD feature enhanced oscillations in several frequency bands in the basal ganglia (BG). Past research has emphasized the enhancement of 13-30 Hz beta oscillations. Recently, however, oscillations in the delta band (0.5-4 Hz) have been identified as a robust predictor of dopamine loss and motor dysfunction in several BG regions in mouse models of PD. In particular, delta oscillations in the substantia nigra pars reticulata (SNr) were shown to lead oscillations in motor cortex (M1) and persist under M1 lesion, but it is not clear where these oscillations are initially generated. In this paper, we use a computational model to study how delta oscillations may arise in the SNr due to projections from the globus pallidus externa (GPe). We propose a network architecture that incorporates inhibition in SNr from oscillating GPe neurons and other SNr neurons. In our simulations, this configuration yields firing patterns in model SNr neurons that match those measured *in vivo*. In particular, we see the spontaneous emergence of near-antiphase active-predicting and inactive-predicting neural populations in the SNr, which persist under the inclusion of STN inputs based on experimental recordings. These results demonstrate how delta oscillations can propagate through BG nuclei despite imperfect oscillatory synchrony in the source site, narrowing down potential targets for the source of delta oscillations in PD models and giving new insight into the dynamics of SNr oscillations.

Keywords Parkinson's disease · Basal ganglia · Conductance-based model · Synaptic inhibition

1 Introduction

Pathological neural oscillations in the basal ganglia and motor cortical brain regions are hallmarks of Parkinson's disease (PD) and have been studied in both Parkinsonian patients and animal models of PD (Boraud et al., 2005; Hammond et al., 2007; Jenkinson & Brown, 2011). Excessive beta oscillations (13-30 Hz) have received much of the attention in the PD literature (Brown et al., 2001; Cassidy et al., 2002; Weinberger et al., 2006; Halje et al., 2019) but lower frequency oscillations have also been observed in PD patients (Levy et al., 2002; Steigerwald et al., 2008; Du et al., 2018; Zhuang et al., 2019) and animal models (Raz et al., 2000; Tseng et al., 2001; Heimer et al., 2006; Walters et al., 2007; Parr-Brownlie et al., 2009; McCairn & Turner, 2009; Aristieta et al., 2016). Such oscillations in human patients have typically been associated with Parkinsonian limb tremor, and while such oscillations can have significant coherence with tremor measured through electromyography (EMG), some oscillating neurons exhibit no such EMG coherence (Du et al., 2018; Hurtado et al., 1999)

Action Editor: Charles Wilson

✉ Jonathan E. Rubin
jonrubin@pitt.edu

Timothy C. Whalen
timcwhalen@gmail.com

John E. Parker
jep220@pitt.edu

Aryn H. Gittis
agittis@cmu.edu

[1] Department of Mathematics, University of Pittsburgh, Pittsburgh, PA, United States

[2] Neuroscience Institute, Carnegie Mellon University, Pittsburgh, PA, United States

[3] Center for the Neural Basis of Cognition, Pittsburgh, PA, United States

[4] Present Address: Design Interactive, Inc., Orlando, FL, United States

or drift in and out of coherence with EMG signals over the course of a recording (Hurtado et al., 2005). These oscillations' relationships to other motor symptoms in PD have been far less studied.

Recently, it was shown that delta oscillations (0.5-4 Hz) are the primary oscillatory phenotype that arises throughout the basal ganglia after loss of dopamine in mouse models of PD whereas, surprisingly, beta oscillations were never observed in these animals (Whalen et al., 2020). In the substantia nigra pars reticulata (SNr), the main output nucleus of the mouse basal ganglia, the prevalence of these delta oscillations is predictive of the severity of dopamine loss and non-tremorous motor dysfunction, and delta oscillations tend to weaken during periods of motor activity. These findings suggest a reappraisal of lower frequency oscillations as a biomarker or causal factor in Parkinsonian akinesia, rigidity and bradykinesia. However, the mechanisms by which these oscillations arise in the Parkinsonian brain are not well-understood.

Parkinsonism subdivides the SNr into two populations defined by their patterns of delta oscillations, as well as a third population of neurons without significant oscillatory activity (Whalen et al., 2020). These two populations exhibit roughly antiphase activity, but when they are referenced to similar pathological oscillations in motor cortex (M1), a clearer picture emerges. One population enters its up-state approximately 180 ms before M1 enters its up-state and is termed active-predicting (AP) because its activity predicts future activity in M1. The second population lags slightly behind, entering its inactive state approximately 120 ms before M1 enters its up-state and is named inactive-predicting (IP) because this population's inactivity predicts M1 activity. These two features - the populations' activity states and lead times relative to M1 - plainly provide a disjoint classification of SNr neurons, but it is not clear how this dichotomy arises in the parkinsonian SNr.

Delta oscillations in the Parkinsonian mouse are known to require the loss of dopaminergic activation of D2 receptors (Whalen et al., 2020). Because of this, a reasonable hypothesis may be that SNr oscillations are inherited from upstream neurons in the indirect pathway of the basal ganglia, which originates in D2-expressing neurons of the striatum. These neurons send inhibitory projections to the globus pallidus externa (GPe), which in turn provides inhibitory projections to the SNr, and GPe neurons themselves exhibit strong delta oscillations in the Parkinsonian state as well. Specifically, the SNr-projecting neurons of the GPe are all part of the so-called prototypic GPe population (Mallet et al., 2012) and exhibit delta oscillations approximately in phase with one another (Mallet et al., 2008).

The main objective of this paper is to test in a computational model whether it is possible for the delta oscillations in GPe to account for the structure of SNr activity that we observe experimentally under dopamine depletion. Specifically, we seek to determine if there exists a GPe-SNr circuit architecture that can reproduce our experimental observations: the presence of near-antiphase AP and IP populations in the SNr and the intrinsic firing patterns and phase relationships observed within these groups. Using data from our previous work (Whalen et al., 2020), we construct confidence intervals for these neural measures that allow comparisons of the results of various simulations to *in vivo* observations. Guided by these comparisons to experimental data, we identify a synaptic architecture that achieves realistic dynamics, and this model's features suggest that a competitive process for GPe and SNr synaptic formation on the somas of SNr neurons is sufficient to allow for the spontaneous generation of AP and IP populations within the SNr when SNr neurons are inhibited with oscillatory GPe input. Despite phase lags within GPe, oscillations arise as observed *in vivo* in the two SNr populations, with inherited phase relations that match experimental data. Moreover, the emergent SNr dynamics persist with temporal drift in the GPe oscillation frequency within the delta band as well as with the inclusion of excitatory inputs from the subthalamic nucleus (STN) to SNr based on recorded STN spike trains. These results suggest that SNr need not develop its own intrinsic oscillations in parkinsonism but can instead inherit them from other basal ganglia nuclei. Overall, these findings provide evidence for the striatum or GPe as the source of parkinsonian delta oscillations, a critical detail in understanding their generation and in designing approaches for their ablation as potential PD treatments.

2 Methods

2.1 *In vivo* experiments and analysis

In this subsection, we discuss the experimental and computational methods that went into the collection and analysis of the experimental data presented in Figs. 1-3 of this paper (cf. Whalen et al. (2020)).

Animals and data collection All experimental data used in this paper were previously published in Whalen et al. (2020), and detailed experimental methods can be found there. In brief, male and female mice on a C57BL/6J background were injected with 6-hydroxydopamine (6-OHDA) into the medial forebrain bundle to induce dopamine depletion (DD); control animals were instead injected with saline. Animals were head-fixed atop a running wheel and acute electrophysiological recordings were performed in the SNr or GPe. Data were manually spike sorted into single units. Some recordings included a simultaneously recorded electrocorticogram

(ECoG) signal measured from primary motor cortex (M1) through an implanted wire.

In this paper, we made use of the experimentally collected GPe and STN data to design the inputs to our model SNr neurons and we utlized the experimentally collected SNr data for direct comparison with the activity of our model SNr neurons. Much of the data analysis used in this paper was already performed and reported in (Whalen et al., 2020), and hence we refer the reader there for the full details of these analysis methods and simply report an abridged version here.

Oscillation detection We detected oscillations by identifying those frequencies at which our data featured both high power and low phase shift. Our power calculations were performed using partially overlapping time segments of 2^{12} ms of data sampled at 1 kHz, with steps of size $\Delta s = 2^9$ ms taken between segments. For each segment, we computed the renewal-corrected PSD as

$$\hat{C}(\omega) = \frac{\hat{C}_\infty(\omega)}{\hat{C}_0(\omega)}$$

and we averaged $\hat{C}(\omega)$ values across segments to obtain the renewal-corrected PSD. Here, $\hat{C}_0(\omega)$ denotes the theoretical power spectral density (PSD) of a renewal process defined by the interspike interval (ISI) probability distribution on the segment scaled by the number of spikes in the segment (Gerstner et al., 2014; Whalen et al., 2020). The numerator term $\hat{C}_\infty(\omega)$ is an estimate of the PSD of the spike train in that segment, given by the squared modulus of the power spectrum of the mean-subtracted spike train in the segment (i.e., the original binary spike train in the segment after subtracting off its mean over that segment, which sets the 0 Hz component of the spectrum to 0). All PSDs in this study have undergone this renewal-correction but are simply referred to as PSDs for brevity.

Our phase shift calculation involved three steps: taking the arctangent of the power spectrum to find an uncorrected phase $\widetilde{\phi}$ at each frequency for each segment; computing a corrected phase ϕ for that frequency and segment by using a mod function and translation to define frequency relative to the start of the recording rather than the start of the segment; and averaging the phases across successive segments for each frequency, to obtain an overall phase shift $\xi(\omega)$ as a function of frequency ω.

Once these calculations had been performed for a recorded unit, we defined statistically significant power to occur at those frequencies within the band 0.5–4 Hz that were local maxima of $\hat{C}(\omega)$, defined as being higher than the three neighboring values to each side, that were above the 99% confidence interval of renewal-corrected power from the region of $\hat{C}(\omega)$ between 250 and 500 Hz, correcting for multiple comparisons (Bonferroni correction) of all frequencies in the delta band. We then checked if any frequency detected in this way had a significantly low phase shift. Such phase shifts were defined as those lying below the 95% confidence interval of phase shifts from the region of $\xi(\omega)$ between 250 and 500 Hz, with correction for multiple comparisons (Bonferroni correction) if multiple frequencies were detected from the PSD.

AP/IP unit classification In recordings with a simultaneous M1 ECoG signal, we built a series of regression models predicting the M1 ECoG signal from the spiking of single SNr units at various lags in order to determine the sign and significance of the relationship between each SNr unit and M1.

First, we binned the ECoG into 10ms bins and defined the dependent variable Y as the difference between adjacent ECoG measurements to reduce nonstationarity. We then built a 10th order autoregressive model of Y which served as the null model. Next, we built additional autoregressive models to test lead/lag relations of SNr unit activity relative to M1. For these models, we calculated the spike density function (SDF) for an SNr unit by convolving its spike train with a Gaussian function with a standard deviation of 100 ms. For simplicity, we assumed that if a lag exists by which the unit firing influences the ECoG or vice versa, then there is only one such lag by which this influence occurs. Thus, for each time shift of the SDF between -1000 and +1000 ms (defined in 10 ms increments, for a total of 201 time shifts) we used the 10th order autoregressive terms and one SDF term with this shift as its explanatory variables.

From this collection, we identified the model with the smallest mean squared error. We next performed an F-test at $\alpha < 0.05$, correcting for 201 comparisons (Bonferroni correction), to determine whether the model at this lag was significantly better than the null autoregressive model. We found that all neurons with a significant lead/lag relationship to M1 exhibited a "best lag" that was negative in time; that is, SNr activity was predictive of future changes in M1. We computed the regression coefficient at this best lag for each neuron. Neurons for which the best lag had a positive coefficient were termed active-predicting (AP), and neurons for which the best lag had a negative coefficient were termed inactive-predicting (IP).

Quantifying phase lags To quantify the oscillation phase lags between pairs of units, we first computed the SDF of each oscillating unit using a Gaussian filter with $\sigma = 50$ ms. For each pair, we performed cross-correlation using a moving window procedure to minimize the effects of nonstationarities in firing rate over the course of the recording (Willard et al., 2019). We used a window size of 20 s with a maximum lag of 4 s and zeroed the first and last 4 s of the one of the SDFs to ensure that the correlation computation at each lag would have an equal amount of zero-padding. We then divided the cross-correlation by its mean at lags greater than 4 s so that the value at each lag could be interpreted as a fraction of the neuron's mean firing rate. This procedure was computed on every window with a moving window step size of 8 s then averaged together to obtain the final normalized cross-correlation between the two signals.

Since most data (and all simulations) did not include an ECoG reference to determine the SNr neuron's identity (AP or IP), we determined that the pair was in the same population if their cross-correlation peak was closer to lag zero than their trough, and different populations if their trough was closer to lag zero than their peak. We defined their relative phase as the absolute value of the lag at which this extreme occurred (whether peak or trough).

2.2 Modeling neuronal dynamics and interactions

Conductance-based model of SNr neurons We used a previously published conductance-based biophysical model of SNr neurons (Phillips et al., 2020) with small modifications noted below. Parameters can be found in Phillips et al. (2020) and were originally adapted from earlier computational studies (Abbott et al., 1997; Corbit et al., 2016; Xia et al., 1998) or tuned from experimental data (Connelly et al., 2010; Zhou et al., 2008), except where otherwise noted.

Because different input sources to SNr neurons have spatially distinct targets, each neuron is modelled with a somatic and a dendritic compartment. The respective membrane potentials V_S and V_D are governed by the equations

$$\begin{aligned} C_S \frac{dV_S}{dt} &= -I_{Na} - I_{NaP} - I_K - I_{Ca} - I_{SK} - I_{leak} \\ &\quad - I_{GABA}^S - I_{DS}, \\ C_D \frac{dV_D}{dt} &= -I_{TRPC3} - I_{SD} - I_{STN}, \end{aligned}$$

where C is that compartment's membrane capacitance and each I is an ion current: fast (I_{Na}) and persistent (I_{NaP}) Na^+ currents, delayed rectifying K^+ current (I_K), Ca^{2+} current (I_{Ca}), Ca^{2+}-activated K^+ current (I_{SK}), leak current (I_{leak}) in the somatic compartment, and a transient receptor potential channel 3 current (I_{TRPC3}) in the dendritic compartment. I_{DS} and I_{SD} are coupling currents representing the current flow from the dendritic to somatic compartments and vice versa. I_{GABA}^S denotes the synaptic current due to projections from simulated GPe neurons (see below) and local connections from other SNr neurons. I_{STN} denotes a tonic excitation from STN, projections from which synapse primarily on dendrites in the SNr (Kita & Kitai, 1987), which is included in lieu of spiking STN neurons. The current equations take the following form:

$$I_{Na} = g_{Na} \cdot m_{Na}^3 \cdot h_{Na} \cdot s_{Na} \cdot (V_S - E_{Na})$$

$$I_{NaP} = g_{NaP} \cdot m_{NaP}^3 \cdot h_{NaP} \cdot (V_S - E_{Na})$$

$$I_K = g_K \cdot n_K^4 \cdot h_K \cdot (V_S - E_K)$$

$$I_{Ca} = g_{Ca} \cdot m_{Ca} \cdot h_{Ca} \cdot (V_S - \alpha \cdot \ln(\frac{[Ca]_{out}}{[Ca]_{in}}))$$

$$I_{SK} = g_{SK} \cdot m_{SK} \cdot (V_S - E_K)$$

$$I_{leak} = g_{leak} \cdot (V_S - E_{leak})$$

$$I_{GABA}^S = g_{GABA}^S \cdot (V_S - E_{GABA}^S)$$

$$I_{DS} = g_C \frac{C_S}{C_S + C_D} \cdot (V_S - V_D)$$

$$I_{TRPC3} = g_{TRPC3} \cdot (V_D - E_{TRPC3})$$

$$I_{SD} = g_C \frac{C_S + C_D}{C_D} \cdot (V_D - V_S)$$

$$I_{STN} = g_{STN} \cdot (V_D - E_{glut})$$

where each g is the current's maximum conductance, each E is the current's reversal potential, and each m, h, n, and s is a gating variable. α in the equation for I_{Ca} is 13.27, the coefficient for calcium in the Nernst equation.

Each of the gating variables obeys an equation of the type

$$\frac{dx}{dt} = \frac{x_\infty(V) - x}{\tau_x(V)}$$

where x is an m, h, n, or s gating variable of a particular current, $x_\infty(V)$ is the gate's steady state and $\tau(V)$ is the gate's time constant, given by

$$x_\infty(V) = (1 + e^{-(V - x_{1/2})/k_x})^{-1},$$

$$\tau_x(V) = \tau_x^0 + \frac{\tau_x^1 - \tau_x^0}{e^{(\tau_{1/2}^x - V)/\sigma_x^0} + e^{(\tau_{1/2}^x - V)/\sigma_x^1}}$$

and all quantities in each expression, other than V, are constants.

An exception to the above specifications arises with the Ca^{2+}-gated SK channel, for which the m gate is governed by

$$m_{SK}([Ca]_{in}) = \left(1 + \left(\frac{k_{SK}}{[Ca]_{in}}\right)^{n_{SK}}\right)^{-1}$$

where k_{SK} is the half-activation calcium concentration and n_{SK} is the Hill coefficient. The intracellular Ca^{2+} concentration $[Ca]_{in}$ evolves according to

$$\frac{d[Ca]_{in}}{dt} = -\alpha_{SK} \cdot I_{Ca} - \left(\frac{[Ca]_{in} - [Ca]_{min}}{\tau_{Ca}}\right)$$

where α_{SK} is a constant relating current to the rate of change of $[Ca^{2+}]_{in}$, τ_{Ca} is the time constant for calcium efflux through Ca^{2+} pumps, and $[Ca]_{min}$ is the minimum calcium concentration at which these pumps are active. The parameters for this equation were adapted from Xia et al. (1998).

The synaptic conductance g^S_{GABA} obeys the equation

$$\frac{dg^S_{GABA}}{dt} = -\frac{g^S_{GABA}}{\tau^S_{GABA}} + W^{GPe}_{GABA} \cdot D \cdot \sum_n \delta(t - t_n) + W^{SNr}_{GABA} \cdot \sum_m \delta(t - t_m)$$

where τ^S_{GABA} is the synaptic decay time constant, W is the synaptic weight from either GPe or other SNr neurons, δ is the delta (impulse) function, and $t_{n,m}$ are the presynaptic spike times arising from GPe and SNr, respectively. D is a scaling factor for short-term synaptic depression governed by (Abbott et al., 1997)

$$\frac{dD}{dt} = \frac{D_0 - D}{\tau_D} - \alpha_D \cdot (D - D_{min}) \cdot \sum_n \delta(t - t_n).$$

We adjusted two of the parameters to represent differences between DD and control conditions. The conductance g_{TRPC3} in DD was set to 0, since activation of D1 receptors is required for the opening of TRPC3 channels in SNr neurons (Zhou et al., 2009). In control conditions, we tuned g_{TRPC3} to match the finding that under Na^+ channel block, blockade of TRPC3 channels yields a 10 mV hyperpolarization of the membrane potential (Zhou et al., 2008). Tuning to respect this fact yielded a value of 0.2 nS/pF for g_{TRPC3} in the control model.

The synaptic conductance g_{STN} was tuned such that the mean firing rate of SNr neurons in the full network model in DD conditions would match the mean firing rate observed *in vivo* in DD. This yielded a range from $0.5 - 2.5$ nS/pF, and the value of g_{STN} for each SNr neuron was selected uniformly from this range at the start of the simulation. Since electrophysiological data reveals a 50% increase in mean STN firing rates in control compared to DD conditions (Whalen et al., 2020), this range was scaled by 1.5 in the control model.

Quadratic integrate-and-fire model To compare our conductance-based model results to those from a simpler framework, we separately modelled SNr neurons as quadratic integrate-and-fire (QIF) units with a tonic excitatory leak current and synaptic inhibition. In this model, each cell's voltage V is governed by

$$dV = [a_0 \cdot (V - V_{rest})^2 - g_{STN} \cdot (V - E_{glut}) - g_{GABA} \cdot (V - E_{GABA})] \cdot dt + \sigma dW$$

where $V_{rest} = -60$; $E_{glut} = 0$ and $E_{GABA} = -70$ are respectively the excitatory and inhibitory reversal potentials; $g_{STN} = 0.001$ is a tonic excitatory conductance tuned to generate realistic SNr firing rates, and g_{GABA} is the inhibitory synaptic conductance defined as g^S_{GABA} in the previous section. Moreover, dW is a Gaussian noise process with standard deviation σ, which was simulated using the Euler-Maruyama method; however, we used a noiseless ($\sigma = 0$) model except where otherwise noted. Finally, for this model, when V reaches a threshold $V_{th} = -20$, the neuron is said to have spiked and V is reset to $V_{reset} = -70$.

Simulated GPe spike trains Rather than simulating GPe neurons in full detail, we generated artificial spike trains to serve as input to the SNr model neurons. In DD, we used GPe spike trains of two types, Poisson or oscillating. Both types were modelled as inhomogeneous Poisson processes with rate function $\lambda(t)$. In Poisson spike trains, the rate function was defined as

$$\lambda(t) = \begin{cases} 0, & t - T \le t_{refrac} \\ \lambda_c, & t - T > t_{refrac} \end{cases}$$

where λ_c is the baseline firing rate, T is the period of the oscillation in milliseconds (ms), and $t_{refrac} = 1$ms is the absolute refractory period. Firing rates were fit to the mean firing rate of GPe neurons recorded experimentally, and since the median GPe firing rate did not differ significantly in control and DD animals (Whalen et al., 2020), λ_c was set to the observed median value of 24 Hz and was unchanged between control and DD simulations.

Oscillating spike trains were defined with a rate function as follows:

$$\lambda(t) = \begin{cases} 0, & t - T \le t_{refrac} \\ \lambda_c + f_{osc}(t, A, \omega), & t - T > t_{refrac} \end{cases}$$

where $f_{osc}(t, A, \omega)$ is a periodic function of time t with frequency ω chosen as 2 Hz to be near the median delta frequency observed in GPe units (Whalen et al., 2020) and amplitude A chosen such that a spike train would have a 1 Hz firing rate at its trough.

Since the delta oscillations observed in the SNr are not perfect sine waves but rather are better fit by oscillatory processes with up and down states, we chose f_{osc} to be a square wave with unequal up and downstate durations; that is,

$$f_{osc}(t, A, \omega) = \begin{cases} A/2, & \bmod(t, 1/\omega) \le u/\omega \\ -A/2, & \bmod(t, 1/\omega) > u/\omega \end{cases}$$

where u is the fraction of each period spent in the upstate. To fit an appropriate value for u, we analyzed the oscillation shapes of GPe neurons recorded *in vivo* in mice (Whalen et al., 2020). We included only neurons with detected oscillations and with firing rates that exceeded 10 Hz to ensure that no arkypallidal neurons were included, as they do not project to SNr (Abdi et al., 2015; Mallet et al., 2012). For each neuron, we computed its spike density function (SDF), sdf(t), by convolving the spike train with a Gaussian filter with σ = 50 ms; this produces a smooth instantaneous firing rate function, but one that is coarse enough such that delta oscillations can still be seen. We then computed a moving mean $\mu(t)$ of the SDF with a rectangular window of 5 s to obtain a mean firing rate over a much longer timescale, but short enough to change along with long-timescale nonstationarities in firing rate. We computed the fraction of time F for which sdf(t) $> \mu(t)$ and found the median F across all neurons to be approximately 0.55. Thus, we chose $u = 0.55$ such that the upstate comprises 55% of each period, while the downstate comprises the remaining 45%.

For simulations in Fig. 4, we allowed ω itself to vary in time. The basic idea of this time variation was to introduce small, random perturbations to ω in a way that preserves history. We implemented this by choosing a long time step, τ_2, and choosing a new sign for the perturbations to ω every τ_2 time units (τ_2 =1000 for Fig. 4A-C and τ_2 =2000 for Fig. 4D-F). In between sign choices, we chose a new perturbation magnitude, $\Delta\omega$, every $\tau_1 < \tau_2$ time units (τ_1 =100 for Fig. 4A-C and τ_1 =500 for Fig. 4D-F). The value of $\Delta\omega$ was chosen from a uniform distribution from 0 to 1% of ω, inclusive (e.g. $\Delta\omega \in [0, 0.02]$ for $\omega = 2$Hz). Once this was selected, we performed the update $\omega \leftarrow \omega \pm \Delta\omega$ where the choice of + or − depended on the most recently chosen perturbation sign.

In the control model, we generated spike trains with a more regular firing pattern, mimicking the firing patterns observed in the healthy GPe (Whalen et al., 2020). Specifically, all neurons in the control model fired spikes with an interspike interval (ISI) of $40 + \epsilon$ ms, with the jitter ϵ for each ISI sampled randomly from a uniform distribution on $[-2, 2]$.

Fitting GPe phase lag distributions Like SNr, oscillations in GPe neurons can exhibit non-zero delays relative to one another. To incorporate these delays into our model, we computed the pairwise phase lag distribution for GPe, as described above for SNr. To simulate a population of neurons with phases such that this distribution was maintained, we sought to estimate the distribution of individual phases from this pairwise phase lag distribution. We assumed that the phases are normally distributed following a normal distribution $N(0, \sigma)$ and sought to estimate σ. The pairwise phase lags that we measured can be considered as the absolute difference of two independent samples from $N(0, \sigma)$, which means that they follow a half-normal distribution $H(0, \sqrt{2\sigma^2})$. The best fit to the pairwise distribution gives an estimate of $\sigma = 34.6164$ ms. At the start of each simulation, a GPe neuron's phase was chosen from this distribution, resulting in a pairwise phase distribution similar to the one observed experimentally.

STN inputs to model SNr neurons In some specific computations, we used experimental STN recordings from Whalen et al. (2020) to simulate STN inputs to the model SNr neurons. For a single simulation of this type, a set of simultaneously recorded STN spike trains were used. The maximal number of simultaneously recorded STN units in the data set was 9, and only those experiments with 8 or 9 simultaneously recorded units were selected. The experimental data was incorporated into the model by defining a dynamic synaptic conductance g^{dyn}_{STN} that evolved according to the equation

$$\frac{dg^{dyn}_{STN}}{dt} = -\frac{g^{dyn}_{STN}}{\tau_{STN}} + W^{STN}_{glut} \cdot \sum_{l} \delta(t - t_l)$$

where $\tau_{STN} = 3ms$ is the synaptic decay time constant, $W_{STN} = 6$ nS/pF is a weight parameter selected such that a jump in g^{dyn}_{STN} from 0 to W_{STN} would induce an increase of about 2 mV in V_D in the absence of other synaptic inputs, δ is again an impulse function, and the t_l are the times at which spikes were observed in any of the simultaneously recorded STN units.

For the simulations that included experimentally-derived STN inputs, we used as the total synaptic conductance $g_{STN} = g^{dyn}_{STN} + g^{stat}_{STN}$, where g^{stat}_{STN} denotes a static bias constant randomly chosen for each SNr neuron from the range 0.13−0.23 nS/pF to maintain appropriate overall SNr firing rates (in contrast to the 0.5−2.5 nS/pF used with static g_{STN}; see Supplemental Fig. 1). For simplicity, the same g^{dyn}_{STN} was used for all SNr neurons in each simulation. For each of the four animals with sufficiently many simultaneously recorded units, we ran four separate simulations, each based on a randomly-selected, 60-second recorded segment. For each of these recordings, we used the first 10 s to allow g^{dyn}_{STN} to equilibrate and incorporated the subsequent 50 s of g^{dyn}_{STN} values into our simulation.

Connection architecture We chose populations of 100 SNr neurons (50 neurons in each population for 2-population models) and 100 GPe spike trains (50 in each of the oscillating and Poisson populations when applicable). Equally sized populations were chosen because the number of neurons in SNr *in vivo* is approximately equal to the number of GPe neurons that project there (Simmons et al., 2020).

We considered several different architectures of connections from GPe to SNr and within SNr. Each SNr neuron received four (in the *basic* and *partially segregated* models) or an average of four (in the *synaptic competition* model) connections from both GPe and other SNr neurons (yielding eight synapses on each neuron in total). The identities of the specific pre-synaptic neurons from a given population that project to each post-synaptic cell were selected completely at random. The other aspects of these models are described when they are discussed in Section 3. These numbers of synapses were chosen since real SNr neurons receive a small number (approximately two to six) unitary connections from GPe (Simmons et al., 2020) and an average of four unitary connections from other SNr neurons (Higgs & Wilson, 2016). While the large strength of these connections is likely due to many synapses from a single presynaptic neuron forming on the postsynaptic neuron (Simmons et al., 2020; Smith & Bolam, 1989), we modelled these nests of boutons as a single, strong synapse from each presynaptic cell. The strength of each synapse was chosen uniformly from the range $0.05 - 0.25$ nS/pF.

2.3 Simulations and analysis

Simulations Code to simulate the models was written in C++. Differential equations were evolved using Euler's method with a timestep of 0.025 ms with data extracted every second time step or, as noted above, with the Euler-Maruyama method when noise was included. Simulations were run for a total of 50 simulation seconds, and the first three seconds were discarded before analysis. Results from the simulation were imported into MATLAB and Python for analysis.

Measuring irregularity with CV_2 Since real spike trains have a greater degree of nonstationarity than those in our simulations, we used the CV_2 measure of irregularity (Holt et al., 1996), which computes the coefficient of variation (CV) over a moving window of two interspike intervals (ISIs), thereby correcting for nonstationarities in firing rate. Specifically, we compute the CV for all pairs of adjacent ISIs and find this distribution's mean:

$$CV_2 = \frac{1}{N}\sum_{i=1}^{N}\frac{2|\Delta t_{i-1} - \Delta t_i|}{\Delta t_{i-1} + \Delta t_i}$$

where Δt_i is the length of the ith ISI and N is the number of adjacent pairs of ISIs in the spike train.

Identifying oscillating neurons Oscillations in single model neurons were detected using the same procedure as used for our spike train data (see *Oscillation detection*), requiring that oscillations passed both the power and phase shift criteria. Although the forcing frequency in our simulations was known to be 2 Hz, our oscillation detection algorithm was agnostic to this information.

Since we did not simulate motor cortex, we could not define AP and IP units in the same manner as in previous experimental work (Whalen et al., 2020). Instead, we compared the phases of SNr oscillations with those in GPe. We computed an SDF of the sum of all GPe neurons' spike trains and calculated the cross-correlation of this mean GPe signal with each SNr neuron that exhibited a delta oscillation. Beyond their relationship to M1, a defining feature of the AP population is that it, on average, leads IP units *in vivo*. Since the only way in our simulations for an oscillation in SNr to become approximately in phase with GPe oscillations would be through a bisynaptic (GPe to SNr to SNr) or higher order multisynaptic connection, we defined AP neurons as those for which the peak in the cross-correlation with the GPe SDF was closer to zero lag than the trough, and IP neurons as those for which the trough was closer to zero lag than their peak. For display purposes, we also defined a phase offset for each neuron relative to GPe. Specifically, for each AP neuron, we computed $\delta = |t_t| - |t_p|$, where t_p, t_t denote the largest peak and trough, respectively, of the cross-correlation between the neuron's SDF and that of the simulated GPe signal. We converted the time δ to a phase by computing $2\pi f\delta$ for f defined as the maximum frequency of the AP neuron's power spectrum. For each IP neuron, we repeated the same process but with $\delta = |t_p| - |t_t|$. All resulting phase offsets were negative, which confirms the validity of the AP/IP classification. We also checked this result by running a simulation of the "basic" model with no GPe phase delays (so lead-lag relationships could be easily identified) and confirming that every neuron defined as AP through this process led every neuron defined as IP. We also confirmed that the AP lead bias remained in our final model (the synaptic competition model, Fig. 3E). While our assumption appears accurate, our computational model neurons may be more accurately referred to as putative AP and IP units; however, in the remainder of this work, we drop the "putative" modifier for brevity.

Quantifying model fit to data To compare the model results to experimental data, we computed means and two-sided 95% confidence intervals for several metrics on the data, such as the firing rate of SNr neurons and the fractions of neurons that exhibited an oscillation. Confidence intervals were computed in one of two ways:

1. The fractions of non-oscillating, AP and IP neurons each follow a binomial distribution $B(p_g)$ with the assumption that each recorded neuron's identity is independent of all others. For each group (AP, IP, or non-oscillating), p_g represents the probability that a neuron is a member of that group. We estimated a 95% confidence interval around the sample mean for each group using the

analytic Clopper-Pearson method implemented in the MATLAB function *binofit*.

2. For all other measures where an analytic estimate was not possible, we computed 1000 bootstrapped samples and calculated the statistic being estimated (e.g. mean or CV), then used the 2.5th and 97.5th percentile from all samples as the 95% confidence interval.

Cluster analysis We examined the separation between the points corresponding to AP and IP neurons on axes defined by either the total synaptic strength from GPe and SNr or the delta power received from GPe and SNr by SNr neurons. To peform this evaluation, we computed the centroids of the AP and IP neuron clusters using labeled data. To quantify the level of cluster separation, we defined a displacement metric, which was calculated for each neuron projected onto the dimension defined by the line connecting the two cluster centroids. Each neuron's displacement was its signed distance from the opposite cluster's centroid, where the direction pointing from the opposite centroid toward the neuron's own cluster's centroid was defined to be positive.

3 Results

We collected *in vivo* data from a variety of basal ganglia regions in mouse (described in detail in previous work (Whalen et al., 2020); see also Methods). These data showed that under DD, two slowly (0.5-4 Hz) oscillating populations of SNr neurons emerge, classified computationally based on whether the active or inactive phase of their oscillations better predicted positive deflections in a simultaneously recorded M1 (motor cortex) ECoG signal, with a near-antiphase relationship between the two (Fig. 1A-B; see also Introduction). In this work, we took the activity of GPe neurons recorded *in vivo* as a starting point, without consideration of its source, and we sought to test the hypothesis that the features of the SNr oscillations observed in experimental data can be explained by a model in which SNr inherits its oscillatory pattern from its GPe inputs, despite the distributed phases of GPe oscillations observed experimentally. To investigate this idea, we built networks of 100 biophysically detailed but simplified SNr neurons receiving input from a collection of 100 simulated GPe spike trains, along with a constant conductance excitatory synaptic input from STN, and compared the results of these simulations to the *in vivo* data from SNr.

3.1 A model with partially segregated pathways matches *in vivo* recordings

To start, we built a model with a simple architecture designed in such a way that two subpopulations of SNr neurons exhibiting antiphase oscillations were likely to emerge. For this model, we split the simulated GPe spike trains into two classes: 50 Poisson spike trains and 50 spike trains with an underlying 2 Hz oscillation in their firing rate (see Section 2). We organized the model SNr neurons into two equal-sized populations, A and B. Population A received synaptic input only from (1) oscillating GPe neurons, and (2) SNr neurons from Population B, whereas Population B received input only from (1) Poisson GPe neurons, and (2) Population A SNr neurons (Fig. 2A). Specific synaptic connections consistent with these constraints were established randomly at the start of the simulation in such a way that each SNr neuron received the same number of synapses, but each GPe train and SNr neuron did not necessarily target the same number of SNr neurons.

To compare the model results with experimentally recorded data, we computed each model SNr neuron's renewal-corrected power spectrum and phase shift (Whalen et al., 2020) to detect neurons with significant delta oscillations, then classified these neurons as either AP or IP based on their activity patterns relative to GPe (Fig. 1C-D; see Section 2). As in the experimental data, offsets of AP neuron SDF peaks were roughly similar to offsets of IP neuron SDF troughs, albeit with some heterogeneity across units.

To continue the comparison with the experimental data, we next compared the delta power of each oscillating model neuron to the delta-band powers of active-predicting (AP) and inactive-predicting (IP) neurons recorded *in vivo* (Fig. 2B-C). Qualitatively, the results of this simulation show a clear AP/IP dichotomy, with group membership determined completely by the neuron's identity in the network architecture. Specifically, those in Population A, which receive oscillatory inhibition from GPe, make up the AP population, while those receiving Poisson inhibition from GPe and thus inheriting their oscillations only from SNr connections make up the IP population. The AP neurons also have greater power than the IP neurons, as seen *in vivo*. The distributions of power levels in the simulations differ substantially from those seen *in vivo*, however, with no overlap between the AP and IP power distributions.

To quantify the fit of our model to experimental data, we checked whether the SNr spike trains in our simulations fell within a 95% confidence interval of metrics derived from real SNr data in three categories: basic firing properties, sizes of oscillatory subpopulations, and properties of oscillations (Fig. 2D).

For basic firing properties, we computed firing rates and regularity of firing quantified with CV_2, a measure of irregularity that corrects for nonstationarities in firing rate over time (see Section 2). In this initial model, the neurons were significantly more regular (CV_2 closer to zero) than in the experimental data.

We next considered the putative identities of neurons: AP, IP, or non-oscillating. In this case, the differences from

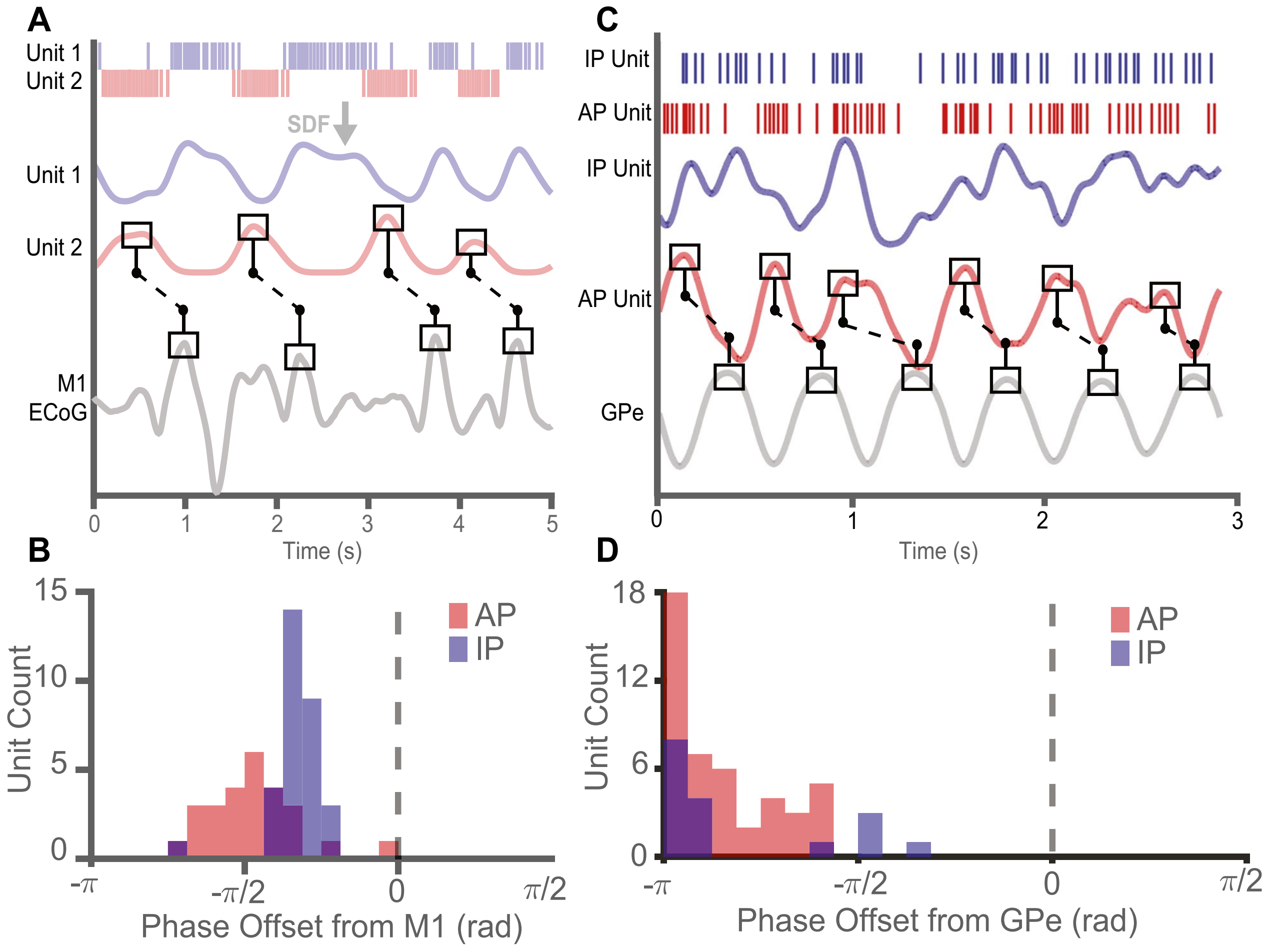

Fig. 1 Experimental data on antiphase oscillations in SNr recorded *in vivo* in DD mice, with corresponding simulation data. **A**. Example data showing how a spike density function (SDF) was used to identify oscillation phases in recorded SNr neurons (AP:red, IP:blue), relative to a simultaneously recorded M1 ECoG signal (grey). **B**. Histogram of phase offsets of $n = 59$ oscillating SNr neurons relative to the M1 ECoG. For AP neurons (red), phase refers to the SDF peak. For IP neurons (blue), phase refers to the SDF trough. A perfectly anti-phase relationship would correspond to complete overlap of these distributions. Figure panels **A**-**B** are reproduced from Figure 8 of our previous paper (Whalen et al., 2020). **C**. SDFs generated from IP (blue) and AP (red) model SNr neurons and from our simulated GPe spike train (grey). Note that consistent with our naming convention, AP peaks lead those in GPe while IP peaks are closer in time to those in GPe. **D**. Histograms of phase offsets of AP peaks (red) and IP troughs (blue) for model neurons, relative to the GPe SDF (see Section 2). The overlapping nature of these distributions captures these two populations' opposing relationships to the GPe

experimental data are stark; since each neuron's identity is determined exactly by which population (A or B) it was assigned to, there are exactly 50 AP and 50 IP neurons with no non-oscillating neurons. Because of this over-simplification, the results completely fail to replicate experimental data on the sizes of the neuronal classes.

Finally, we examined some properties of the oscillations exhibited by the model AP and IP neurons. Note that the underlying oscillations in our simulations are stationary (i.e. they are exactly a function of time, so their autocorrelations do not decay at long lags), whereas oscillations in the experimental setting have an autocorrelation that decays to zero after a few periods. It is thus difficult to compare raw power values between the simulations and experimental data; as such, we computed a mean power ratio between the AP and IP classes, defined as the ratio between the mean power of all AP neurons and the mean power of all IP neurons in the simulation at the forcing frequency from GPe, a measure which should cancel out the differences in stationarity between the experimental and simulated data. We found that in terms of the mean power ratio, this model matches experimental data in that AP neuron oscillations are stronger than IP neuron oscillations. However, the strength disparity that emerged in our simulations is significantly less than that found *in vivo*. We also computed the CVs of the power of oscillations across neurons in each population to determine if the variability of oscillation strengths across neurons matched the real data. In the basic model results,

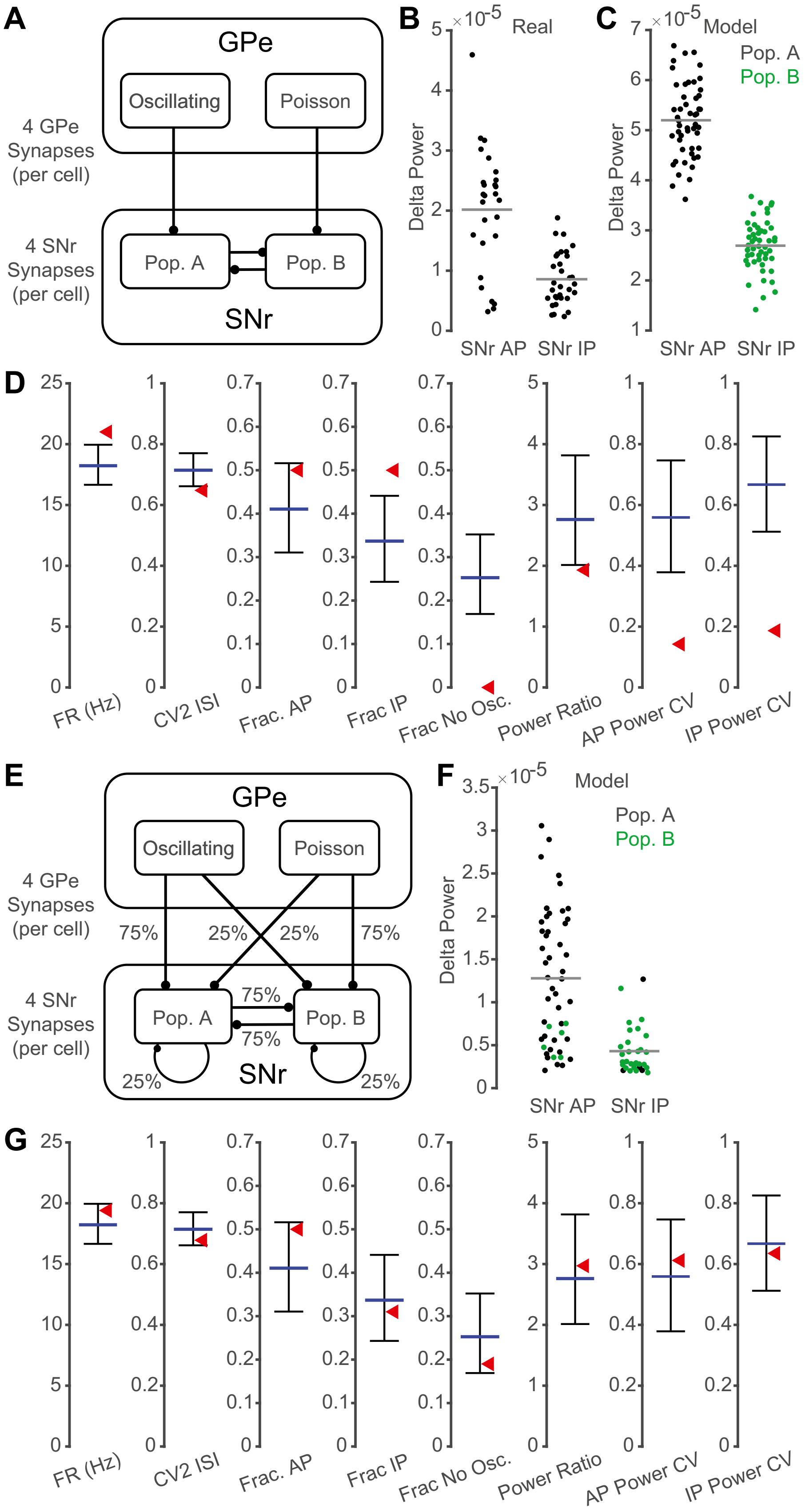

Fig. 2 Performance of models with segregated pathways. **A**. Architecture for the *basic* model, where two SNr populations receive inputs from two entirely distinct GPe subpopulations (one oscillating, one Poisson) and only project to each other. **B**. Delta power of each neuron *in vivo* in the AP and IP SNr populations. **C**. As in B, but from the results of a simulation of the basic model. Black dots are neurons from Population A from the architecture in Panel A, green dots are neurons from Population B. **D**. Performance of the basic model on measures derived from *in vivo* data. Each bar is a bootstrapped or analytically derived confidence interval (see Section 2) and each red arrow is the model's results computed from all simulated SNr neurons. FR: mean firing rate (Hz); CV2 ISI: mean CV$_2$ of interspike intervals; Frac AP/IP/No Osc: fraction of neurons in the AP, IP, or non-oscillating populations. Power Ratio: ratio of the mean delta power of all AP neurons to the mean power of all IP neurons. AP/IP Power CV: CV of the distribution of AP/IP delta powers. **E**. Architecture for the *partially segregated* model, which extends the basic model to include probabilities of connections crossing over from the population they would normally project to. **F**-**G**. Same as **C**-**D** for the results from the partially segregated model

there is significantly less variability in oscillation strength in both populations than *in vivo*.

Overall, this basic model's primary deviation from experimental data lies in the variability of the oscillations that SNr neurons exhibit. Specifically, in this model, all neurons within a population oscillate at similar intensities, whereas neurons *in vivo* have more varied oscillations or may show no detectable oscillations at all. As such, we reject the hypothesis that the experimentally observed SNr activity features arise from a fully segregated architecture of GPe-SNr and SNr-SNr connections. As an alternative, we extended our model to include additional variability by relaxing its strict connectivity rules. Instead of all Population A neurons receiving input only from oscillating GPe neurons and from Population B SNr neurons, we included a "crossover probability" such that 25% of Population A's GPe synapses instead came from Poisson neurons and 25% of its SNr synapses were from other Population A neurons. This adjustment was mirrored in Population B: 25% of GPe synapses to Population B were now from the oscillating population and 25% of SNr synapses were from Population B. We termed this the *partially segregated model* (Fig. 2E).

We found that the partially segregated model yields AP and IP populations in the SNr with much more realistic delta power distributions than observed in the original model (Fig. 2F). Notably, a neuron's phase outcome was not determined completely by whether it was in Population A or B as was the case in the basic model; by chance, some Population A neurons have an IP relationship to GPe rather than the expected AP relationship, and vice versa for Population B. This model also performed significantly better quantitatively than did the original, as each of the properties we measured falls within the confidence intervals derived from experimental data (Fig. 2G). The small number of crossover connections led to weaker oscillations in some neurons, thereby increasing the breadth of oscillation strengths seen in each population and leading to the absence of detectable oscillations in some neurons, presumably due to the combination of synaptic inputs that they received.

3.2 A less prescribed synaptic competition model also matches *in vivo* recordings

While it fits experimental data better than the basic model, the partial segregation model still assumes the existence of two anatomically distinct populations in SNr that are biased to receive inputs of specific types from GPe and fellow SNr neurons. To relax this assumption, we considered an architecture that could potentially allow for such a dichotomy to emerge through natural heterogeneity. This model features a single heterogeneous population of SNr neurons that each receive a total of 8 synapses, each arising from a GPe spike train or an SNr neuron source with equal likelihood. We term this the *synaptic competition model* in keeping with the traditional use of "synaptic competition" to refer to the competition for space on individual postsynaptic targets (Cancedda & Poo, 2009), as GPe and SNr (randomly) compete to make synapses on each SNr neuron (Fig. 3A). Note, however, that there is no competition-based constraint on the weights of those connections that are present in the network. With this model, we posited that the neurons that, by chance, had a high level of inhibition from GPe would form the basis of the AP population and those with a high level of inhibition from those AP neurons would form the IP population, while neurons receiving more balanced input would fall to one side or the other through more complicated multisynaptic dynamics or would not oscillate at all.

Simulations of the synaptic competition model showed generally similar results to the partial segregation model. The synaptic competition model produces fractions of AP and IP SNr neurons and distributions of delta power in the AP and IP populations (Fig. 3B) that are similar to those of the partial segregation model, although with weaker power intensities than previously. Moreover, all quantitative measures computed from SNr activity characteristics for the synaptic competition model fall within the confidence intervals determined from *in vivo* data (Fig. 3C).

The evident delta oscillations and emergence of antiphase populations in SNr occurred *in vivo* exclusively under DD conditions. Having identified a model that captured the basic properties of the data and had a reasonably simple and realistic architecture, we asked if a version of this model that did not include properties associated with DD would reasonably fit our control *in vivo* data. As such, we made three modifications to the synaptic competition model: 1) Instead of oscillating and Poisson spike trains, all simulated spike trains from GPe were tuned to be approximately pacemaking (see Section 2); 2) the passive TRPC3 current was strengthened, consistent with experimental findings (Zhou et al., 2008, 2009); 3) the tonic STN synaptic excitation to model SNr neurons was increased as observed under healthy conditions in our *in vivo* data. Without any additional parameter tuning, the SNr dynamics of this model produced the SNr firing rates and variability observed *in vivo* in healthy animals (Fig. 3D). As such, this model of competitive synaptic allocation in SNr from GPe and other SNr neurons matches our SNr data in both the control and dopamine depleted conditions. These results suggest that a competitive synapse formation mechanism could allow the SNr, when subject to low-frequency oscillatory input from GPe, to exhibit two distinct clusters of oscillating neurons.

3.3 Imperfectly synchronous GPe oscillations partially propagate and promote phase lag dichotomy in SNr

Next, we sought to delve deeper into some of the dynamics of the synaptic competition model with conductance-based model neurons in DD. First, we investigated the phase delays between neurons within and between AP and IP populations. A feature of the *in vivo* AP/IP dichotomy is that oscillations in AP neurons tend to lead those in IP neurons (Whalen et al., 2020). Since we do not have an M1 reference signal in the model as we did in some of our *in vivo* data, we attempted to replicate this finding using the cross-correlations between spike trains from individual neurons (see Section 2). Using all of our labeled pairs of simultaneously recorded AP and IP neurons, we see a clear bias towards AP neurons leading simultaneously recorded IP neurons (Fig. 3E, p = 0.0179, Wilcoxon signed rank test). In our results from the synaptic competition model (in which we can simulate many more pairs of simultaneously recorded neurons), we see a similar bias toward the AP population leading IP neurons (Fig. 3F, $p < 0.0001$).

We also compared the more general distributions of within-population and between-population pairwise phase lags. In our experimental data, both distributions peaked at zero, as expected. While the within-population distribution has a sharper peak in the real data than in our simulated results (indicating that our simulation has slightly inflated lags relative to the real data), the distributions are not significantly different from one another (Fig. 3G, p = 0.2850, two-sample Kolmogorov-Smirnov test). Similarly, the between-population distributions in both the real and simulated data are wider than the within-population distributions, and the simulation is again not significantly different from the real data (Fig. 3H, p = 0.1443). As such, this model replicates the phase delays evident in the DD SNr network, although it may be biased slightly towards longer delays.

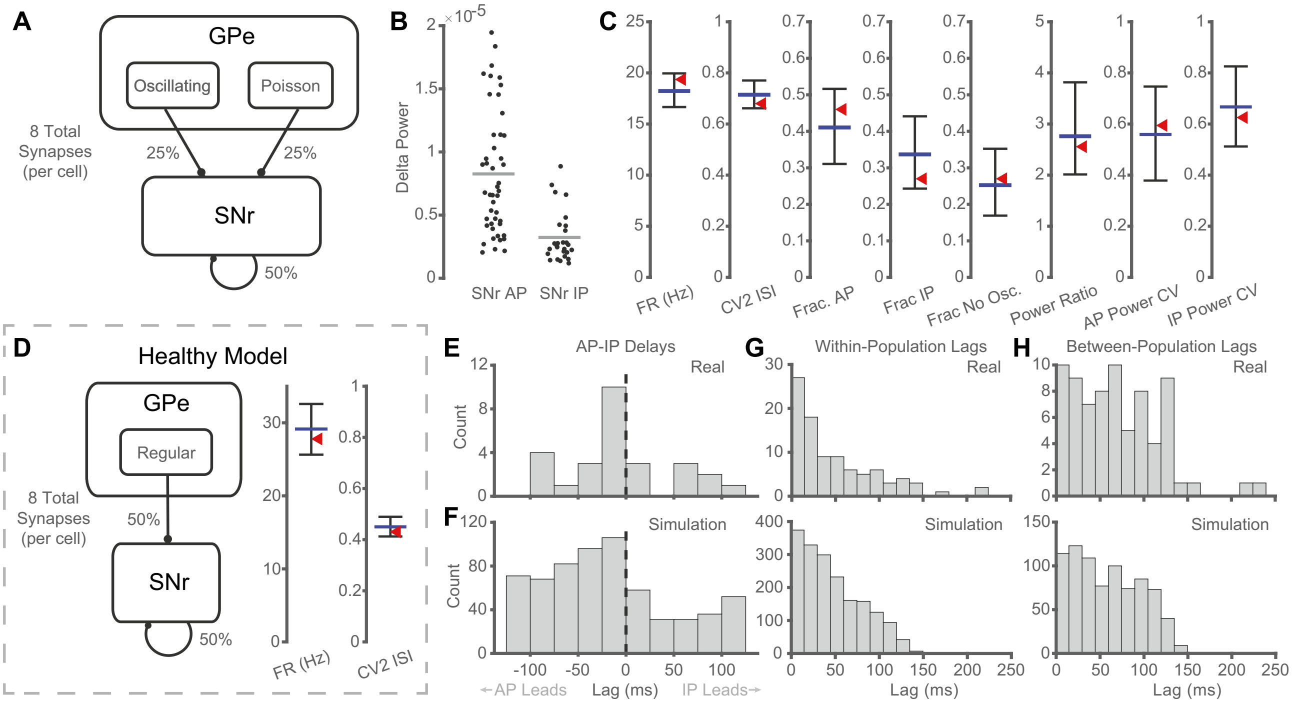

Fig. 3 Performance of the synaptic competition model. **A**. Architecture for the "competitive" model, where the numbers of GPe and SNr synapses onto each SNr neuron are not fixed, but each SNr neuron's fixed total number of synapses have an equal chance of arising from GPe or SNr. **B**. Delta power for each neuron in the AP and IP populations from a simulation of the synaptic competition model. **C**. Performance of the synaptic competition model on measures derived from *in vivo* data, see Fig. 2C. **D**. Left: Architecture of the healthy version of the synaptic competition model where all oscillating and Poisson GPe neurons are replaced with pacemakers. Right: Same as **C**, but only comparing to measures from control *in vivo* data and only looking at measures which do not depend on the presence of delta oscillations. **E**. Analysis of AP/IP lead-lag relationship. Histogram of the phase lags between all pairs of simultaneously recorded AP and IP neuron pairs *in vivo*. Counts on the left indicate AP leading IP. **F**: Same as E for the results of the synaptic competition model. **G**. Analysis of broader lead-lag relationships. Top: histogram of the absolute phase lags between all pairs of neurons in the same population (putatively AP vs. AP or IP vs. IP). Bottom: same as top for the results of the synaptic competition model. **H**. Same as **G** for all pairs of neurons in opposite populations (putatively AP vs IP)

3.4 Oscillations persist under stochastic variations in frequency but not in higher frequency bands

We performed additional simulations with the synaptic competition model to test whether transmission of oscillations would persist when the oscillation frequency varied over time (see Section 2). With a 2Hz baseline frequency ω, this temporal variation had little impact on the measures of SNr activity that we consider in this work (Fig. 4). On the other hand, when we increased ω into the beta band, with or without temporal variations, the oscillations in the input signal no longer achieved the same degree of entrainment of the SNr population. Specifically, we find far fewer AP SNr neurons and many more non-oscillatory SNr units with higher frequency input oscillations; for example, Fig. 4 shows representative results for $\omega = 15$Hz, and we obtained very similar results with $\omega = 20, 25$, and 30Hz as well. Hence, we conclude that the mechanisms at work in the model in this paper yield low frequency signal transmission but do not extend up to frequencies in the beta band. We will return to this effect again in Section 3.7 and in the Section 4.

3.5 Results are robust to the inclusion of STN inputs to SNr

Delta oscillations were also observed in the STN *in vivo* in DD mice (Whalen et al., 2020), so excitatory inputs from STN to SNr could play a role in determining the dynamics in SNr. To provide an initial exploration of this point, we augmented the synaptic competition model to include dynamic STN inputs to the SNr neurons, based on experimental recordings. Specifically, we generated an excitatory synaptic current in the dendrite of each model SNr neuron, with a dynamic conductance that jumped by a fixed amount at each time that a spike was fired by any of a collection of simultaneously recorded STN neurons and decayed exponentially between spikes (see Section 2). We ran a total of 16 simulations that included dynamic STN inputs, produced by picking 4 random time segments from each of the 4 recorded animals.

We found that although the inclusion of these dynamic input currents from STN to SNr significantly altered the specific timing of the spikes generated by the model SNr neurons, it had little impact on the model SNr neurons' oscillation properties (Fig. 5). These results were robust across

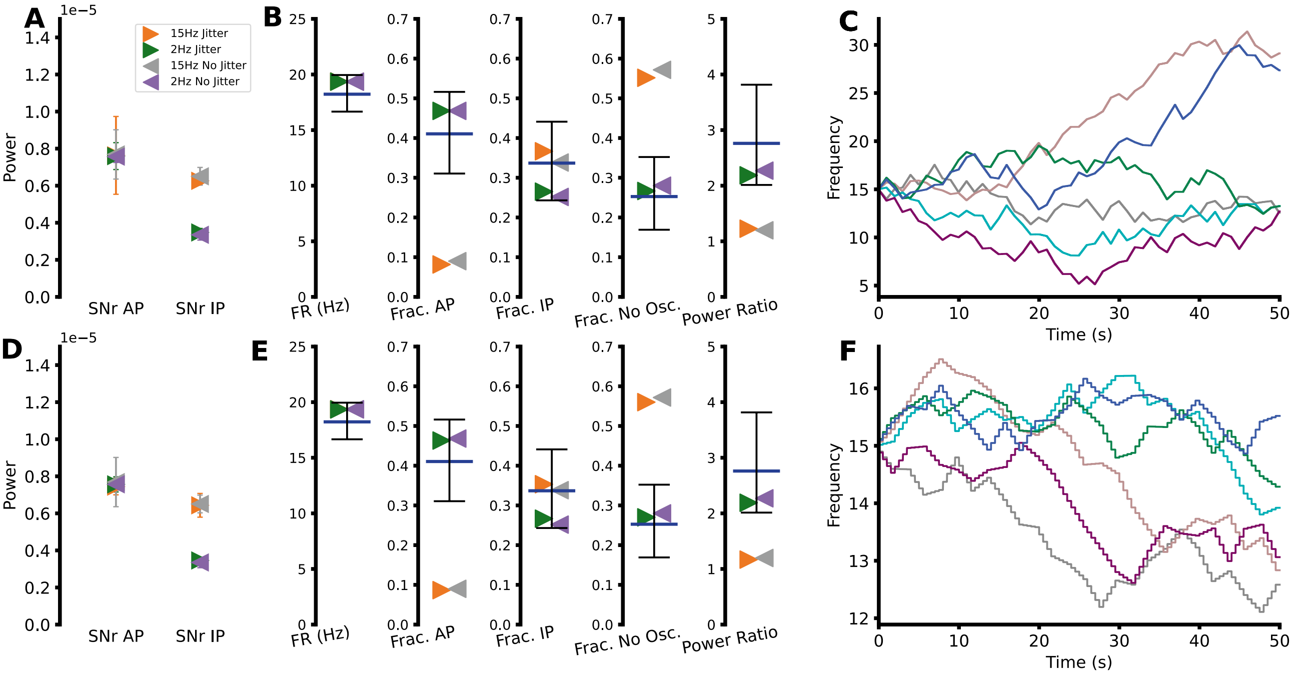

Fig. 4 Performance of the synaptic competition model with varying frequencies of input oscillations. **A**. Power in the SNr AP and IP clusters for $\omega = 2$Hz and $\omega = 15$Hz with and without fast variation ($\tau_1 = 100$ and $\tau_2 = 1000$) in ω. **B**. Similar comparison across model performance measures. Note that the 2Hz results persist under variation in ω whereas the larger ω yields quite different results, including a lack of significant oscillations in about 60% of SNr neurons. **C**. Six randomly selected examples of the time courses of ω used in **A-B** for the 15Hz baseline. **D-F**. Similar results with a slower variation ($\tau_1 = 500$ and $\tau_2 = 2000$) in ω

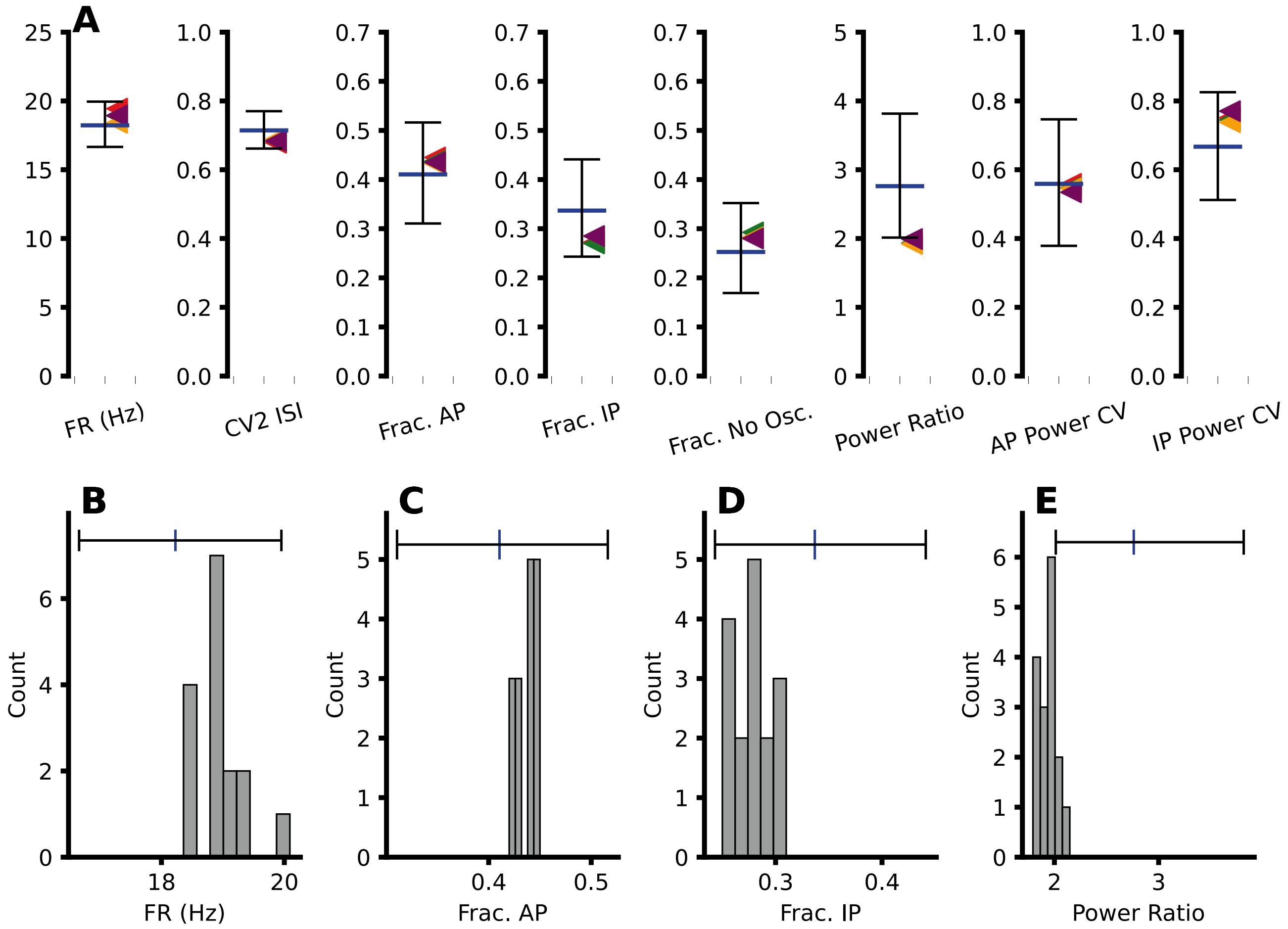

Fig. 5 Results of including experimental STN data in the simulated SNr network. **A**. Comparison across model performance measures as in Figs. 2, 3, 4. Each data point (colored triangle) represents the results averaged over four simulations corresponding to four different STN data samples from one animal. **B**. Histogram of average firing rates across the SNr network for all 16 simulations where STN data was included. The horizontal bar is the experimental data confidence interval of the respective measure, with the median marked in blue. **C**-**E**. Same as **B** but for: (**C**) the fraction of SNr neurons in the AP oscillation cluster (Frac. AP), (**D**) the fraction of SNr neurons in the IP oscillation cluster (Frac. IP), and (**E**) the ratio of the mean delta power in the AP cluster to that in the IP cluster, respectively

the 16 trials. Thus, these simulations are consistent with the idea that GPe oscillations are a possible source of the delta oscillations observed in the SNr, in which anti-phase relationships emerge locally within the SNr, with STN inputs affecting overall SNr firing rates but not providing a primary influence on SNr oscillations.

3.6 A simplified SNr neuron model replicates some, but not all, *in vivo* results

To check the generality of our results, and in particular whether they rely on some specific nonlinearities associated with SNr intrinsic dynamics or rather emerge simply from the properties and connection pattern of the synapses, we repeated our simulations of the synaptic competition model with the conductance-based SNr neural model replaced with quadratic integrate-and-fire (QIF) neurons (see Section 2).

We obtained similar results after this model substitution with regards to the size, strength and power variability of the AP and IP populations (Fig. 6A-B). The one measure on which the QIF model does not match *in vivo* recordings or the conductance-based model is the variability of ISIs, measured using CV_2. To increase this variability closer to levels observed *in vivo*, we added Gaussian noise to the QIF voltage equation (see Section 2) at varying levels to see how this modification impacted our results. While increases in voltage noise increased ISI irregularity to within the confidence interval derived from *in vivo* data, there was a commensurate increase in the fraction of non-oscillating neurons and decrease in the ratio of AP:IP power, each of which fell out of their confidence intervals (Fig. 6C). These results demonstrate that the configuration of synaptic connections is a key component of the underlying oscillatory dynamics in this system, but the nonlinearities of the conductance-based

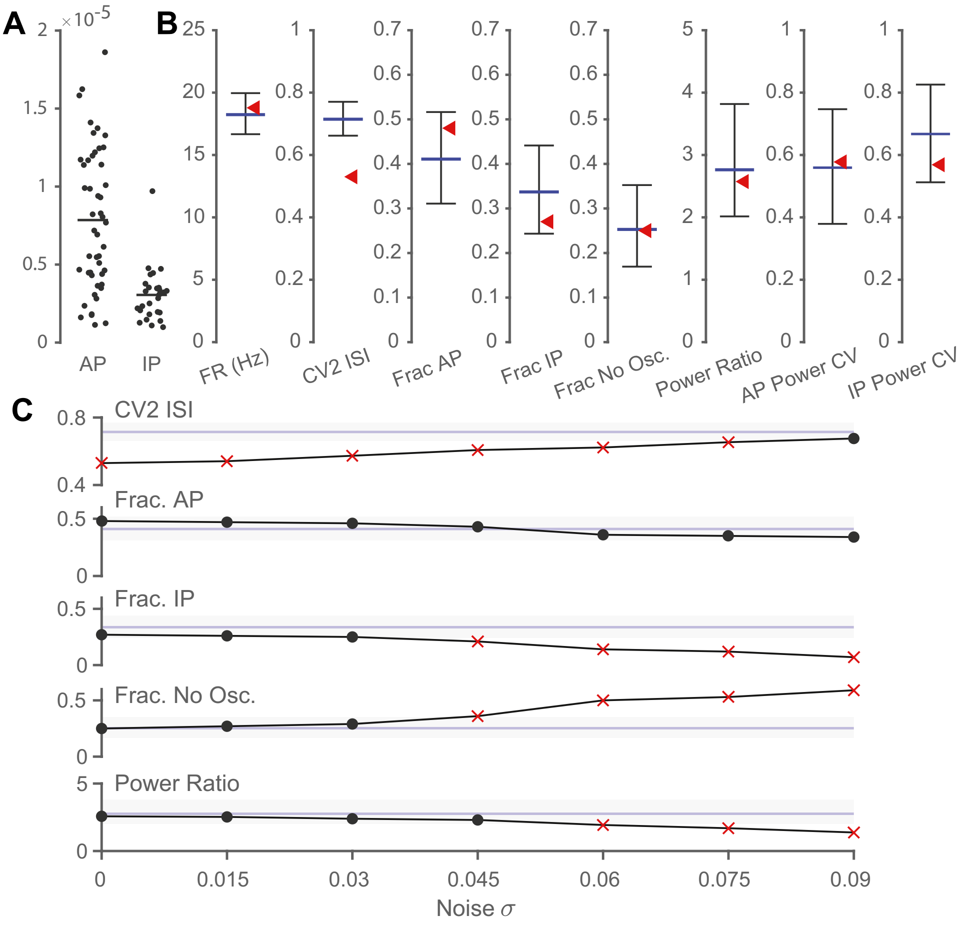

Fig. 6 Performance of the synaptic competition model with simplified SNr dynamics based on the QIF model. **A**. Delta power for each neuron in the AP and IP populations from a simulation of the synaptic competition model using QIF SNr neurons. **B**. Performance of the synaptic competition model with QIF neurons on measures derived from *in vivo* data, see Fig. 2C. **C**. Performance of the model on select measures from panel **B** with increasing levels of Gaussian noise in the QIF voltage equation. Black circles indicate that the measure at that noise level fell within the confidence interval derived from real data (grey band), red X's indicate a result which fell outside the confidence interval. From top to bottom: CV_2 of ISIs, fraction of AP oscillating neurons, fraction of IP oscillating neurons, fraction of non-oscillating neurons, and the ratio of the mean power of the AP and IP populations

model are important for reproducing a complete picture of the SNr neural dynamics.

3.7 The power of oscillatory inputs from GPe and SNr define the AP and IP clusters

Finally, we sought to understand more deeply the dynamics leading to the distinct AP and IP populations in our synaptic competition model. Since the number of synapses that each SNr neuron receives from either population (GPe or SNr) follows a unimodal binomial distribution, we might expect a continuous spectrum of oscillatory profiles, with a large number of non-oscillating neurons receiving near-equal numbers of GPe and SNr synapses while neurons on the tails of this distribution express a strong AP or IP oscillation. The large numbers of strongly oscillating AP and IP neurons arising in our simulations, however, suggest that the neurons' intrinsic dynamics and synaptic interactions may combine to separate units into the more distinct AP and IP classes.

To investigate this idea, for each neuron, we plotted the sum of its synaptic weights from GPe against the sum of its synaptic weights from other SNr neurons. As expected, these two measures have an inverse relationship as dictated by the competition between the number of GPe and SNr synapses on a single neuron built into the model. Additionally, we see that AP neurons tend to receive more GPe input while IP neurons tend to receive more SNr input, as expected (Fig. 7A). Note that each neuron's placement on this scatterplot is determined completely by the random setup of the network, as no synaptic weights are changed during the simulation. As such, there is an expected binomial-like, unimodal density of points along the $y = -x$ line.

Next, we weighed each synaptic weight by its oscillatory power at the forcing frequency (2 Hz) to visualize the total oscillatory power each neuron receives from GPe and SNr synapses. Here, we see the AP and IP neurons separate into much more distinct clusters (Fig. 7B). To quantify this effect, we computed the distance from each point to the centroid of the other cluster, in the direction specified by the line connecting the two cluster centroids, and found the distribution of these distances to be biased to the positive side of zero (Fig. 7C). As a comparison, we performed the same distance computation on the strength scatterplot in Fig. 7A and found a distance distribution more shifted toward zero, as would be expected from this visually unimodal 2-D distribution

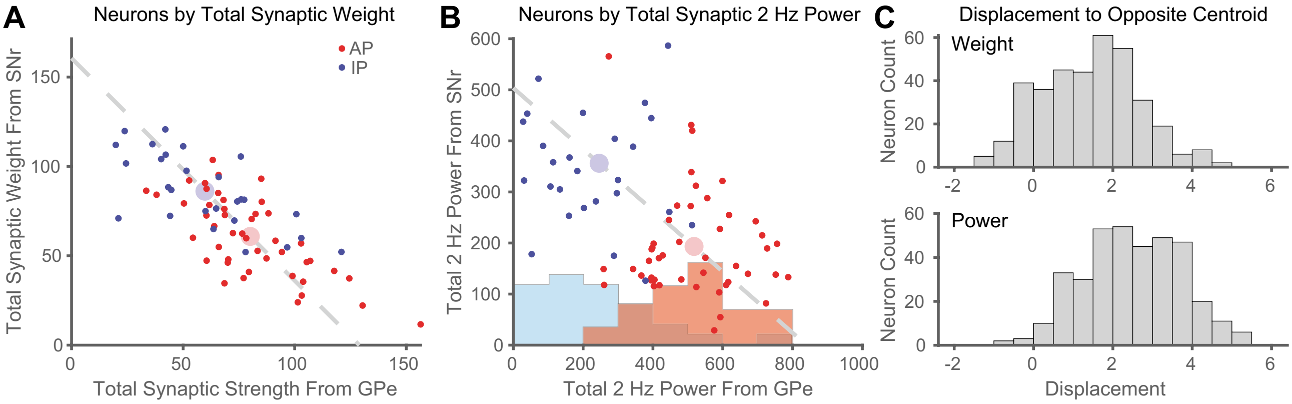

Fig. 7 Model SNr neurons cluster based on presynaptic GPe and SNr delta power. **A**. Scatterplot of AP (red) and IP (blue) neurons based on their total synaptic strength from other SNr and GPe neurons. The two larger, lighter circles denote the centroids of the AP and IP clusters. **B**. Same as **A**, except plotting the total 2 Hz power (Σ[(2 Hz power) × (synaptic strength)]) from SNr and GPe. Also, histograms show marginal distributions of 2Hz power from GPe for the IP and AP clusters. **C**. Top: Displacement (signed distance) of each neuron in the GPe-SNr synaptic strength space (panel A) to the centroid of the opposite (AP or IP) cluster along the dimension defined by the line connecting the two centroids (grey dashed line in A), totaled over 5 runs of the synaptic competition model with different randomly instantiated connections and strengths. Bottom: Same as top for the neurons in the GPe-SNr synaptic delta power space (panel B)

(Fig. 7C). This degree of separation of clusters is surprising, as it is not clear how the levels of presynaptic oscillatory power received by each neuron would dichotomize to push these clusters apart, in contrast to the unimodality that we observe in the strength scatterplot. This finding demonstrates that the neurons in this model undergo an unexpected bifurcation into two mostly distinct AP and IP populations, which are not purely dictated by the synaptic architecture in the network nor by the level of 2Hz power neurons receive from GPe. Finally, we saw in Fig. 4 that inputs with higher frequency oscillations are less effective at inducing peaks at similar frequencies in the SNr neurons, with a major loss of AP SNr neurons. A similar analysis to Fig. 7B done with the higher frequency oscillations (Supplemental Fig. 2) illustrates the lack of high frequency power in the GPe input signal to SNr neurons in the 15 Hz case, which apparently translates into a failure to shut down SNr neurons rhythmically and push them into the AP phase relationship with their inputs (Fig. 1C), perhaps because the inhibitory signal resulting from imperfectly synchronized inputs at these higher frequencies averages out to be less variable (see also Section 4).

4 Discussion

In this work, we have demonstrated that slowly oscillating firing rates in a subset of GPe neurons suffice to induce an oscillation structure in the SNr that mimics *in vivo* experimental observations under DD (Whalen et al., 2020). These results occur in a *partially segregated* network architecture that explicitly defines SNr subdivisions by their distinct synaptic connectivity patterns, where neurons tend to fall into AP- or IP-like phase relationships based on which of the two architectural subdivisions they belong to. However, we show that this dichotomy is also possible through a simpler and less assumptive *synaptic competition model* wherein SNr and GPe compete to form a limited number of synapses on each SNr soma. With small, experimental data-driven changes to simulate a healthy state, we show that the model exhibits firing rates and patterns that match what we observe in healthy control mice, lending further credence to the realism of our model. Importantly, our results demonstrate that despite the imperfect synchrony of delta oscillations in GPe, these oscillations can propagate to downstream targets and generate oscillations with realistic phase distributions in SNr. Moreover, these findings persist when excitatory STN inputs to SNr neurons based on recorded spike trains are included in our simulations and when the inhibitory input oscillation frequency drifts over time, whereas the widespread, clustered nature of the SNr oscillations significantly deteriorates when this input frequency is shifted to the beta band.

Our results are rather intuitive, but multiple aspects of these findings are non-trivial: (a) The most straightforward architecture for producing anti-phase dynamics, the segregated architecture shown in Fig. 2A, does not reproduce the variability in the data. (b) In the successful partially segregated model shown in Fig. 2E, the cluster membership of some neurons does not match what would be expected from the synaptic architecture alone. (c) The biological reasonable but non-segregated synaptic competition model shown in Fig. 3A can completely capture the anti-phase oscillations in the data. (d) Despite a mild phase heterogeneity in GPe, significant phase differences emerge between the SNr clusters. (e) The cluster membership in the synaptic competition model is not entirely determined by the total oscillatory power from the GPe; the histograms in Fig. 7B show the significant overlap between the clusters on this measure. (f) This work shows that imperfectly synchronized oscillations can propagate across populations via inhibitory synapses, which do not necessarily provide the straightforward signal transmission associated with excitatory synapses.

Network architecture assumptions Our initial models assumed two anatomically distinct populations of SNr neurons receiving connections from specific types of GPe and SNr cells. Specifically, we assumed that the synaptic targets of oscillating and Poisson neurons in GPe are predominantly members of distinct neuron pools in SNr and that these two SNr populations primarily project to one another rather than to themselves. Experimentally, there is clear evidence of topographical pathways through the basal ganglia, including the GPe-SNr pathway, which are segregated by the higher order processes – motor, limbic, or associative – with which they are associated (DeLong & Wichmann, 2010; Yelnik et al., 2002). The topography is likely more complicated, continuous, and convergent, however, than the two discrete populations that we define in this model (Foster et al., 2020; Nakano, 2000). Given experimental results demonstrating the connection between delta oscillations and motor symptoms (Whalen et al., 2020), it is possible that oscillations may be restricted primarily to motor pathways in the basal ganglia while not penetrating limbic or associative pathways, which could lend credence to our built-in dichotomy, although there is no direct evidence for this idea. Even if two distinct GPe-SNr pathways exist as we have modelled them here, however, it is unlikely that the two SNr populations would be more likely to project to each other rather than back to themselves, and this is a critical detail for our basic and partially segregated models' oscillatory behaviors. As such, we consider these initial models a proof of concept for how realistic oscillations could form in such a system, but not necessarily a realistic model of the GPe-SNr network.

In contrast, our synaptic competition model does not rely on any of these assumptions. Instead, the only architectural assumption made is the existence of competition between GPe and SNr neurons for the formation and maintenance of synapses on SNr somas. While to our knowledge there is no direct evidence of this competition at this site, other examples of similar synaptic competition exist. For example, synaptic scaling occurs in many regions of the brain to approximately balance a neuron's output (Turrigiano, 2008), although this has primarily been studied at excitatory rather than inhibitory synapses, and nascent synapses may be pruned if nearby synapses are particularly active (Lo & Poo, 1991). Notably, SNr neurons tend to exhibit large nests of synapses all arising from the same presynaptic neuron (Simmons et al., 2020; Smith & Bolam, 1989); this redundancy may explain the atypical strength of these connections onto SNr, and could also increase synaptic competition if the physical space for multiple synaptic nests is limited. While studies have looked closely at the synaptic connectivity from GPe to SNr and within SNr (Higgs & Wilson, 2016; Simmons et al., 2020), no study has looked at the relationships between these connections and whether strong inhibition from one source affects the probability of receiving strong inhibition from the other. A study directly testing whether levels of inhibition from GPe and SNr on a single SNr neuron are inversely correlated, as we have predicted here, would lend credence to our proposed model of delta oscillation propagation from GPe to SNr.

Model simplifications, predictions, and possible extensions In comparing the results from models to real data, we ran statistical tests or derived confidence intervals to determine if the simulated results were statistically indistinguishable from the real data in a classical statistical sense. We caution, however, that our failure to reject the null hypothesis that our simulation produces distributions that are the same as those observed *in vivo* is not an acceptance of that null hypothesis. Such a claim can, in fact, never be proven, as even two samples from identical distributions will never have precisely the same mean (or any test statistic of interest). For the purposes of this study, we consider these techniques sufficient to claim that our model reasonably matches the experimental results.

With any computational model, certain aspects of realism must be sacrificed, both in the model construction and in interpreting its results. We focused our study on a network of conductance-based SNr model neurons, which grounds this model in biological realism based on the known ionic currents driving these neurons' electrochemical dynamics and allows them to be well fit to experimental data. As we demonstrated through a contrasting experiment with simpler QIF model neurons, the complexity of dynamics afforded by conductance-based neurons is important to capture the full breadth of neural patterns we considered in this study.

Even our relatively realistic conductance-based model, however, entails many simplifications. We included only two compartments, one somatic and one dendritic, such that the model neglects features like dendritic computation and variable or even failed propagation of action potentials down an axon. While we include short-term synaptic depression, longer term plasticity is neglected, due both to the complexity that this would induce in the model and a lack of experimental understanding of plasticity in the SNr.

Additionally, certain newly discovered aspects of GPe and SNr physiology could have significant implications if included in this model. While GPe is canonically an inhibitory nucleus, it has been shown to have both inhibitory and excitatory effects on SNr neurons (Freeze et al., 2013; Phillips et al., 2020), the latter of which may result from a shift in the chloride reversal potential due to high chloride influx derived from the many sources of inhibitory input to SNr (Phillips et al., 2020). Such shunting or excitatory effects of GPe inputs could greatly shift how effectively oscillations propagate from GPe to SNr, especially in a model in which chloride dynamics are allowed to dynamically shift E_{Cl}. A sufficiently depolarized E_{Cl} can in fact allow for the spontaneous emergence of delta oscillations in a network of interconnected SNr neurons (Phillips et al., 2020). These oscillations are much weaker than those we see *in vivo*, exhibiting only approximately a 2 Hz difference between peak and trough compared to the complete cessation of firing observed in many SNr neurons *in vivo*. Nonetheless, this intrinsic drive to oscillate at a delta frequency under certain conditions could make SNr more effective at amplifying oscillations present in the synaptic inputs that it receives from other nuclei or could be the initial source of these oscillations, which are subsequently amplified by other biophysical mechanisms or through a multisynaptic loop (e.g. Corbit et al., 2016; Rubin, 2017). Indeed, the delta power that the SNr populations exhibit in our synaptic competition model is not as strong as that in the data (compare Fig. 2B versus Fig. 3B), and some sort of amplification mechanism outside the scope of our model may be responsible for this discrepancy.

While we use the term *synaptic competition model* for the connection architecture that we propose, we caution that the particulars of such synaptic competition have been ignored here. We assume that there is limited space for the large synaptic nests that are made on SNr somas (Simmons et al., 2020; Smith & Bolam, 1989), and we begin the model at a state in which that limited space has already been allocated to GPe and SNr neurons. The endpoint of this inferred competition can be tuned in the model by adjusting the probability that a unitary connection arises from GPe rather than SNr, but the details of how that underlying competition might occur in the brain are not considered. In biological neurodevelopment, such competition could exist in many forms, with synapses being formed, pruned, strengthened, and weakened through a number of activity-dependent plasticity mechanisms (Fino et al., 2005; Thoenen, 2000), or the synapses could genuinely be distributed in a simple random fashion. The details of such development and plasticity in the SNr are not known, but do not affect the endpoint of the system that we are modeling here.

Despite these simplifications, we find that our model performs well at capturing the structure of the oscillatory dynamics across the SNr that are seen experimentally (Whalen et al., 2020). To truly determine the usefulness of this model, it is important to tie its results to predictions that can be checked experimentally to test its veracity.

A major conclusion of our work is that oscillations in GPe are sufficient to recreate the oscillations observed experimentally in SNr. This hypothesis could be tested by comparing the oscillatory power in SNr neurons before and after the ablation of GPe. We caution, however, that while GPe may be sufficient to entrain SNr in this way, it may not be the only nucleus doing so. Interestingly, while delta oscillations have been observed in the STN (Whalen et al., 2020) in DD mice, our results show that these are not necessary to explain the emergent SNr dynamics and that inclusion of STN inputs based on recorded spike trains has little impact on the qualitative dynamics of SNr neurons in the synaptic competition model; however, a more thorough exploration of the impact of STN inputs on SNr dynamics remains for future work. For example, we supply the same STN inputs to all of our model SNr neurons, but in reality, some heterogeneity in connectivity will surely be present. Moreover, since STN and D1 neurons from striatum both synapse onto SNr dendrites, there could exist a competitive level of innervation between these two populations. The effects that such architectures have on the resulting dynamics in SNr could suggest which pattern of connections from STN to SNr may actually occur *in vivo*. The direct pathway inputs from striatal neurons themselves could also play a role in establishing the oscillation structure in SNr, although these neurons were not observed to exhibit delta oscillations (Whalen et al., 2020). Furthermore, changes in SNr intrinsic properties, in extracellular ion concentrations (cf. Phillips et al. (2020)), in neuromodulation, and in other biophysical factors could also contribute to SNr oscillations in DD. Finally, another related future step would be to use a previously developed model GPe-STN network, known to produce oscillations under simulated parkinsonian conditions (Terman et al., 2002), as the source of inputs to the model SNr neurons. This step would first require tuning of the GPe-STN model to capture the features of the experimentally observed delta oscillations (Whalen et al., 2020).

Propagation of imperfectly synchronous delta oscillations A particularly interesting result in our simulations is the effective entrainment of a large subset of SNr neurons by GPe despite the imperfect synchrony of GPe oscillations, along with the separation of SNr neurons into distinct phase clusters with larger differences in oscillation phases. Regarding the latter feature, it appears that the IP sub-population inherits its oscillations from the AP sub-population, with a delay based on the recovery time for IP from inhibition from AP. The mechanism by which the SNr population splits into distinct clusters despite the continuum of levels of low-frequency power that the neurons receive (Fig. 7B) is not yet clear, however. Our *in vivo* recordings of GPe neurons reveal a spread in the times when their delta peaks occur. We posit that the reason that phase-shifted GPe oscillations can effectively integrate in a single SNr neuron in a manner that causes oscillatory firing is that the phase differences still represent only a fraction of the slow oscillation period and that the heterogeneity of phases merely changes the shape of the resultant oscillation; for instance, in the case of square wave oscillatory profiles, oscillations with a large delay integrated in the same SNr neuron may simply change the relative durations of the neuron's up and down states while still allowing the delta oscillation to express. Indeed, in simulations with higher frequency oscillations in the GPe spike trains, we did not observe the same degree of signal propagation and splitting of SNr neurons into two phase-shifted clusters that we obtained with delta oscillations.

Taking this idea one step farther, we hypothesize that the presence of relatively large phase differences in GPe may help explain why delta oscillations are such a strong feature in DD. A 20 ms delay between two neurons undergoing a 1 Hz oscillation still keeps them approximately in phase, covering only 1/50 of their cycle. Yet, the same delay in, for example, a 25 Hz oscillation gives these neurons an antiphase relationship. If lags of this size are a common feature of neural oscillations regardless of the oscillation frequency, due to jitter across neurons in the times at which they switch between spiking up and non-spiking down states, heterogeneity in intrinsic neuronal properties and coupling, or other factors, then a group of neurons oscillating at the same high frequency would essentially tile the phase space, so the integration of these signals in downstream neurons would undergo destructive interference, making the propagation of these high frequency oscillations difficult. This idea suggests that delta oscillations may be particularly robust to the natural variability in relative timing across neurons within a population, and could help explain why they can have such a strong synchronizing effect, entraining the entire cortex during slow-wave sleep (Steriade et al., 1993) and extending throughout the basal ganglia, as we have established in mice (Whalen et al., 2020), in DD.

Supplementary Information The online version contains supplementary material available at https://doi.org/10.1007/s10827-023-00853-z.

Acknowledgements We thank Ryan Phillips for providing the C++ code upon which our biophysical model was based and for helpful discussions regarding our changes and tuning of the finished model. We also thank Charles J. Wilson for suggesting the comparison with the integrate-and-fire model.

Funding This work was partially supported by NSF award DMS 1951095 (JER) and by NIH awards R01DA053014 (JER), R01NS125914 (JER/AHG), R01NS101016 (AHG), R01NS104835 (AHG), and F31NS101821 (TCW).

Data availability No new data was utlized in this work.

Code availability Computational model and analysis code is currently available at the following site: https://github.com/jparker25/Whalen_et_al_2021

Declarations

Conflict of interest The authors declare no conflict of interest.

References

Abbott, L. F., Varela, J., Sen, K., & Nelson, S. (1997). Synaptic depression and cortical gain control. *Science, 275*(5297), 221–224.

Abdi, A., Mallet, N., Mohamed, F. Y., Sharott, A., Dodson, P. D., Nakamura, K. C., Suri, S., Avery, S. V., Larvin, J. T., Garas, F. N., et al. (2015). Prototypic and arkypallidal neurons in the dopamine-intact external globus pallidus. *Journal of Neuroscience, 35*(17), 6667–6688.

Aristieta, A., Ruiz-Ortega, J., Miguelez, C., Morera-Herreras, T., & Ugedo, L. (2016). Chronic l-dopa administration increases the firing rate but does not reverse enhanced slow frequency oscillatory activity and synchronization in substantia nigra pars reticulata neurons from 6-hydroxydopamine-lesioned rats. *Neurobiology of Disease, 89*, 88–100.

Boraud, T., Brown, P., Goldberg, J. A., Graybiel, A. M., Magill, P. J. (2005). Oscillations in the basal ganglia: the good, the bad, and the unexpected. In: *The basal ganglia VIII*, Springer, pp 1–24

Brown, P., Oliviero, A., Mazzone, P., Insola, A., Tonali, P., & Di Lazzaro, V. (2001). Dopamine dependency of oscillations between subthalamic nucleus and pallidum in parkinson's disease. *Journal of Neuroscience, 21*(3), 1033–1038.

Cancedda, L., & Poo, M. M. (2009). Synapse formation and elimination: competition and the role of activity. In: Binder M, Hirokawa N, Windhorst U (eds) *Encyclopedia of Neuroscience,* Springer, Berlin, Heidelberg, pp 3932–3938

Cassidy, M., Mazzone, P., Oliviero, A., Insola, A., Tonali, P., Lazzaro, V. D., & Brown, P. (2002). Movement-related changes in synchronization in the human basal ganglia. *Brain, 125*(6), 1235–1246.

Connelly, W. M., Schulz, J. M., Lees, G., & Reynolds, J. N. (2010). Differential short-term plasticity at convergent inhibitory synapses to the substantia nigra pars reticulata. *Journal of Neuroscience, 30*(44), 14854–14861.

Corbit, V. L., Whalen, T. C., Zitelli, K. T., Crilly, S. Y., Rubin, J. E., & Gittis, A. H. (2016). Pallidostriatal projections promote β oscillations in a dopamine-depleted biophysical network model. *Journal of Neuroscience, 36*(20), 5556–5571.

DeLong, M., & Wichmann, T. (2010). Changing views of basal ganglia circuits and circuit disorders. *Clinical EEG and neuroscience, 41*(2), 61–67.

Du, G., Zhuang, P., Hallett, M., Zhang, Y. Q., Li, J. Y., & Li, Y. J. (2018). Properties of oscillatory neuronal activity in the basal ganglia and thalamus in patients with parkinson's disease. *Translational neurodegeneration, 7*(1), 1–13.

Fino, E., Glowinski, J., & Venance, L. (2005). Bidirectional activity-dependent plasticity at corticostriatal synapses. *Journal of Neuroscience, 25*(49), 11279–11287.

Foster, N. N., Korobkova, L., Garcia, L., Gao, L., Becerra, M., Sherafat, Y., Peng, B., Li, X., Choi, J. H., Gou, L., et al. (2020). The mouse cortico-basal ganglia-thalamic network. bioRxiv

Freeze, B. S., Kravitz, A. V., Hammack, N., Berke, J. D., & Kreitzer, A. C. (2013). Control of basal ganglia output by direct and indirect pathway projection neurons. *Journal of Neuroscience, 33*(47), 18531–18539.

Gerstner, W., Kistler, W. M., Naud, R., Paninski, L. (2014). Neuronal dynamics: From single neurons to networks and models of cognition. Cambridge University Press

Halje, P., Brys, I., Mariman, J. J., da Cunha, C., Fuentes, R., & Petersson, P. (2019). Oscillations in cortico-basal ganglia circuits: Implications for parkinson's disease and other neurologic and psychiatric conditions. *Journal of Neurophysiology, 122*(1), 203–231.

Hammond, C., Bergman, H., & Brown, P. (2007). Pathological synchronization in parkinson's disease: networks, models and treatments. *Trends in Neurosciences, 30*(7), 357–364.

Heimer, G., Rivlin, M., Israel, Z., Bergman, H. (2006). Synchronizing activity of basal ganglia and pathophysiology of parkinson's disease. *Parkinson's Disease and Related Disorders*, pp 17–20

Higgs, M. H., & Wilson, C. J. (2016). Unitary synaptic connections among substantia nigra pars reticulata neurons. *Journal of Neurophysiology, 115*(6), 2814–2829.

Holt, G. R., Softky, W. R., Koch, C., & Douglas, R. J. (1996). Comparison of discharge variability *in vitro* and *in vivo* in cat visual cortex neurons. *Journal of Neurophysiology, 75*(5), 1806–1814.

Hurtado, J. M., Gray, C. M., Tamas, L. B., & Sigvardt, K. A. (1999). Dynamics of tremor-related oscillations in the human globus pallidus: a single case study. *Proceedings of the National Academy of Sciences, 96*(4), 1674–1679.

Hurtado, J. M., Rubchinsky, L. L., Sigvardt, K. A., Wheelock, V. L., & Pappas, C. T. (2005). Temporal evolution of oscillations and synchrony in gpi/muscle pairs in parkinson's disease. *Journal of Neurophysiology, 93*(3), 1569–1584.

Jenkinson, N., & Brown, P. (2011). New insights into the relationship between dopamine, beta oscillations and motor function. *Trends in Neurosciences, 34*(12), 611–618.

Kita, H., & Kitai, S. (1987). Efferent projections of the subthalamic nucleus in the rat: light and electron microscopic analysis with the pha-l method. *Journal of Comparative Neurology, 260*(3), 435–452.

Levy, R., Ashby, P., Hutchison, W. D., Lang, A. E., Lozano, A. M., & Dostrovsky, J. O. (2002). Dependence of subthalamic nucleus oscillations on movement and dopamine in parkinson's disease. *Brain, 125*(6), 1196–1209.

Lo, Y. J., & Poo, M. M. (1991). Activity-dependent synaptic competition *in vitro*: heterosynaptic suppression of developing synapses. *Science, 254*(5034), 1019–1022.

Mallet, N., Pogosyan, A., Márton, L. F., Bolam, J. P., Brown, P., & Magill, P. J. (2008). Parkinsonian beta oscillations in the external globus pallidus and their relationship with subthalamic nucleus activity. *Journal of Neuroscience, 28*(52), 14245–14258.

Mallet, N., Micklem, B. R., Henny, P., Brown, M. T., Williams, C., Bolam, J. P., Nakamura, K. C., & Magill, P. J. (2012). Dichotomous organization of the external globus pallidus. *Neuron, 74*(6), 1075–1086.

McCairn, K. W., & Turner, R. S. (2009). Deep brain stimulation of the globus pallidus internus in the parkinsonian primate: local entrainment and suppression of low-frequency oscillations. *Journal of Neurophysiology, 101*(4), 1941–1960.

Nakano, K. (2000). Neural circuits and topographic organization of the basal ganglia and related regions. *Brain and Development, 22*, 5–16.

Parr-Brownlie, L. C., Poloskey, S. L., Bergstrom, D. A., & Walters, J. R. (2009). Parafascicular thalamic nucleus activity in a rat model of parkinson's disease. *Experimental Neurology, 217*(2), 269–281.

Phillips, R. S., Rosner, I., Gittis, A. H., & Rubin, J. E. (2020). The effects of chloride dynamics on substantia nigra pars reticulata responses to pallidal and striatal inputs. *Elife, 9*, e55592.

Raz, A., Vaadia, E., & Bergman, H. (2000). Firing patterns and correlations of spontaneous discharge of pallidal neurons in the normal and the tremulous 1-methyl-4-phenyl-1, 2, 3, 6-tetrahydropyridine vervet model of parkinsonism. *Journal of Neuroscience, 20*(22), 8559–8571.

Rubin, J. E. (2017). Computational models of basal ganglia dysfunction: the dynamics is in the details. *Current Opinion in Neurobiology, 46*, 127–135.

Simmons, D. V., Higgs, M. H., Lebby, S., & Wilson, C. J. (2020). Indirect pathway control of firing rate and pattern in the substantia nigra pars reticulata. *Journal of Neurophysiology, 123*(2), 800–814.

Smith, Y., & Bolam, J. P. (1989). Neurons of the substantia nigra reticulata receive a dense gaba-containing input from the globus pallidus in the rat. *Brain Research, 493*(1), 160–167.

Steigerwald, F., Potter, M., Herzog, J., Pinsker, M., Kopper, F., Mehdorn, H., Deuschl, G., & Volkmann, J. (2008). Neuronal activity of the human subthalamic nucleus in the parkinsonian and nonparkinsonian state. *Journal of Neurophysiology, 100*(5), 2515–2524.

Steriade, M., McCormick, D. A., & Sejnowski, T. J. (1993). Thalamocortical oscillations in the sleeping and aroused brain. *Science, 262*(5134), 679–685.

Terman, D., Rubin, J. E., Yew, A., & Wilson, C. (2002). Activity patterns in a model for the subthalamopallidal network of the basal ganglia. *Journal of Neuroscience, 22*(7), 2963–2976.

Thoenen, H. (2000). Neurotrophins and activity-dependent plasticity. *Progress in Brain Research, 128*, 183–191.

Tseng, K. Y., Kasanetz, F., Kargieman, L., Riquelme, L. A., & Murer, M. G. (2001). Cortical slow oscillatory activity is reflected in the membrane potential and spike trains of striatal neurons in rats with chronic nigrostriatal lesions. *Journal of Neuroscience, 21*(16), 6430–6439.

Turrigiano, G. G. (2008). The self-tuning neuron: synaptic scaling of excitatory synapses. *Cell, 135*(3), 422–435.

Walters, J. R., Hu, D., Itoga, C. A., Parr-Brownlie, L. C., & Bergstrom, D. A. (2007). Phase relationships support a role for coordinated activity in the indirect pathway in organizing slow oscillations in basal ganglia output after loss of dopamine. *Neuroscience, 144*(2), 762–776.

Weinberger, M., Mahant, N., Hutchison, W. D., Lozano, A. M., Moro, E., Hodaie, M., Lang, A. E., & Dostrovsky, J. O. (2006). Beta oscillatory activity in the subthalamic nucleus and its relation to dopaminergic response in parkinson's disease. *Journal of Neurophysiology, 96*(6), 3248–3256.

Whalen, T. C., Willard, A. M., Rubin, J. E., & Gittis, A. H. (2020). Delta oscillations are a robust biomarker of dopamine depletion severity and motor dysfunction in awake mice. *Journal of Neurophysiology, 124*(2), 312–329.

Willard, A. M., Isett, B. R., Whalen, T. C., Mastro, K. J., Ki, C. S., Mao, X., & Gittis, A. H. (2019). State transitions in the substantia nigra reticulata predict the onset of motor deficits in models of progressive dopamine depletion in mice. *Elife, 8*, e42746.

Xia, X. M., Fakler, B., Rivard, A., Wayman, G., Johnson-Pais, T., Keen, J., Ishii, T., Hirschberg, B., Bond, C., Lutsenko, S., et al. (1998). Mechanism of calcium gating in small-conductance calcium-activated potassium channels. *Nature, 395*(6701), 503.

Yelnik, A. P., Lebreton, F. O., Bonan, I. V., Colle, F. M., Meurin, F. A., Guichard, J. P., & Vicaut, E. (2002). Perception of verticality after recent cerebral hemispheric stroke. *Stroke, 33*(9), 2247–2253.

Zhou, F. W., Matta, S. G., & Zhou, F. M. (2008). Constitutively active trpc3 channels regulate basal ganglia output neurons. *Journal of Neuroscience, 28*(2), 473–482.

Zhou, F. W., Jin, Y., Matta, S. G., Xu, M., & Zhou, F. M. (2009). An ultrashort dopamine pathway regulates basal ganglia output. *Journal of Neuroscience, 29*(33), 10424–10435.

Zhuang, P., Hallett, M., Meng, D., Zhang, Y., & Li, Y. (2019). Characteristics of oscillatory activity in the globus pallidus internus in patients with parkinson's disease (p1.8-028). *Neurology, 92*(15 Supplement).